LA-UR-16-20205
Approved for public release; distribution is unlimited.

Title: Los Alamos and Lawrence Livermore National Laboratories Code-to-Code Comparison of Inter Lab Test Problem 1 for Asteroid Impact Hazard Mitigation

Author(s): Weaver, Robert P.
Miller, Paul
Howley, Kirsten
Ferguson, Jim Michael
Gisler, Galen Ross
Plesko, Catherine Suzanne
Managan, Rob
Owen, Mike
Wasem, Joseph
Bruck-Syal, Megan

Intended for: Report

Issued: 2016-01-15

Title:
Los Alamos and Lawrence Livermore National Laboratories Code-to-Code Comparison of Inter Lab Test Problem 1 for Asteroid Impact Hazard Mitigation

Authors:
Weaver, Robert P. (082050) , XTD-IDA: XTD INTEGRATED DESIGN & ASSESSMENT
Miller, Paul, LLNL: WCI
Howley, Kirsten, LLNL: WCI
Ferguson, Jim Michael (287520) , XTD-PRI: XTD PRIMARY PHYSICS
Gisler, Galen Ross (090091) , XTD-IDA: XTD INTEGRATED DESIGN & ASSESSMENT
Plesko, Catherine Suzanne (146863) , XTD-NTA: XTD NUCLEAR THREAT ASSESSMENT
Managan, Rob, LLNL: WCI
Owen, Mike, LLNL: WCI
Wasem, Joseph, LLNL: WCI
Bruck-Syal, Megan, LLNL: WCI

Los Alamos and Lawrence Livermore National Laboratories Code-to-Code Comparison of Inter Lab Test Problem 1 for Asteroid Impact Hazard Mitigation

LANL Project Lead: Robert Weaver[1], LLNL Project Lead: Paul Miller[2],
Report Editor: Kirsten Howley[2]

ABSTRACT (*P. Miller*)

The NNSA Laboratories have entered into an interagency collaboration with the National Aeronautics and Space Administration (NASA) to explore strategies for prevention of Earth impacts by asteroids. Assessment of such strategies relies upon use of sophisticated multi-physics simulation codes. This document describes the task of verifying and cross-validating, between Lawrence Livermore National Laboratory (LLNL) and Los Alamos National Laboratory (LANL), modeling capabilities and methods to be employed as part of the NNSA-NASA collaboration. The approach has been to develop a set of test problems and then to compare and contrast results obtained by use of a suite of codes, including MCNP, RAGE, Mercury, Ares, and Spheral. This document provides a short description of the codes, an overview of the idealized test problems, and discussion of the results for deflection by kinetic impactors and stand-off nuclear explosions.

[1]Los Alamos National Laboratory, P.O. Box 1663, Los Alamos, NM 87545; rpw@llnl.gov; +1(505) 667-4756

[2]Lawrence Livermore National Laboratory, P.O. Box 808, Livermore, CA 94551; [miller3, howley1]@llnl.gov; +1(925) 42[3-6455, 2-9150]

Contents

1. Motivation (*K. Howley*)

The National Nuclear Security Agency (NNSA) and the National Aeronautics and Space Administration (NASA) have joined in an interagency collaboration to study mitigation strategies for diverting objects on Earth-impact trajectories. While a suite of methods have been proposed to deflect these objects, nuclear explosions and kinetic impactors have been identified as two effective methods to mitigate a potential impact, especially when the object is large or the time to impact is short. These two methods work by delivering an impulse that either deflects or disrupts a body. Numerical simulations provide a means for estimating the response of objects to these impulses in a variety of scenarios. This modeling requires a detailed understanding of various target compositions, sizes and shapes, the energy coupling and response of target material, and the numerical accuracy of the simulations.

To verify our modeling capabilities of the effects of nuclear explosions and kinetic impactors on asteroid-like objects, two of NNSA's laboratories, Los Alamos National Laboratory (LANL) and Lawrence Livermore National Laboratory (LLNL), have developed an inter-laboratory test problem, coined Inter Lab Test Problem 1 (ILTP1). The purpose of ILTP1 is to calculate and compare the deflection velocity for a two-dimensional (2D) test object using stand-off nuclear explosions of various energies and a kinetic impactor. Test Problem 1n (ILTP1n) compares stand-off neutron sources, Test Problem 1x (ILTP1x) compares stand-off x-ray sources, and Test Problem 1i (ILTP1i) compares a kinetic impactor. Yields ranging from 20 kT to 1 MT are explored for the stand-off nuclear test cases. The stand-off nuclear explosion case employing neutrons compares the effect of higher energy neutrons vs. lower energy neutrons, and the x-ray case compares the effect of a warmer spectrum to a cooler spectrum. The kinetic impactor case uses a 1 ton impactor at 10 km/s, corresponding to a kinetic energy of 0.01 tons of TNT equivalent.

2. Physics Codes

2.1. The Monte Carlo N-Particle Transport Code, MCNP (LANL, *J. Ferguson*)

The well-known Monte Carlo Neutral Particle transport simulation package MCNP is used to estimate energy deposition for both neutrons and photons, which yields the angular and radial distribution profiles for energy coupling. The radiation transport from the source to the asteroid is modeled using the particle-transport code MCNP (LANL). MCNP does not calculate thermal, nor hydrodynamic responses of the material, however it does take into account the energy dependence of the radiation as it interacts with the material, and can thus calculate how much energy (heat) is deposited into which portion of the material. Figure 1 displays how the total cross-section and material heating depend on particle energy of the neutrons (left plot) and photons (right plot) on log-log plots, for silicon (Si) and oxygen (O_2). The two vertical lines in each figure represent the appropriate particle energies: 2.45 MeV and 14.1 MeV for the neutrons; 1 keV and 2 keV

for the photons. The particles are transported from the source with their appropriately specified initial energy, through vacuum (void), until they reach the asteroid and begin scattering, which causes the particles to change energy, thus depositing heat into the material with each scatter. Again, MCNP does not calculate the material's thermal response, but only the amount of heat the particles deposit by scattering, and where the heat is deposited. MCNP calculates where the heat is deposited by defining cell volumes and tabulating (tallying) all scattering events in each volume. Assuming that the atomic density, $n = 0.0798363\,[\text{atoms/cm}^3]$, of the asteroid is constant, the heat deposited for a collision, $q\,[\text{MeV/cm}^3]$, is the product of the atomic density and the heating number, $\chi\,[\text{MeV/collision}]$, thus the heat deposited for a flux of particles is the product of the atomic density, the heating number, the particle flux, $\Phi\,[\text{particles/cm}^2]$, and the total cross section, $\sigma_t\,[\text{cm}^2]$. In formal notation, the heat deposited within a volume, is:

$$q = \frac{1}{V}\int_V dV \int_E dE \int_{4\pi} d\Omega \left[\sigma_t\left(E\right)\Phi\left(r, E, \Omega\right) n\,\chi\left(E\right)\right] . \tag{1}$$

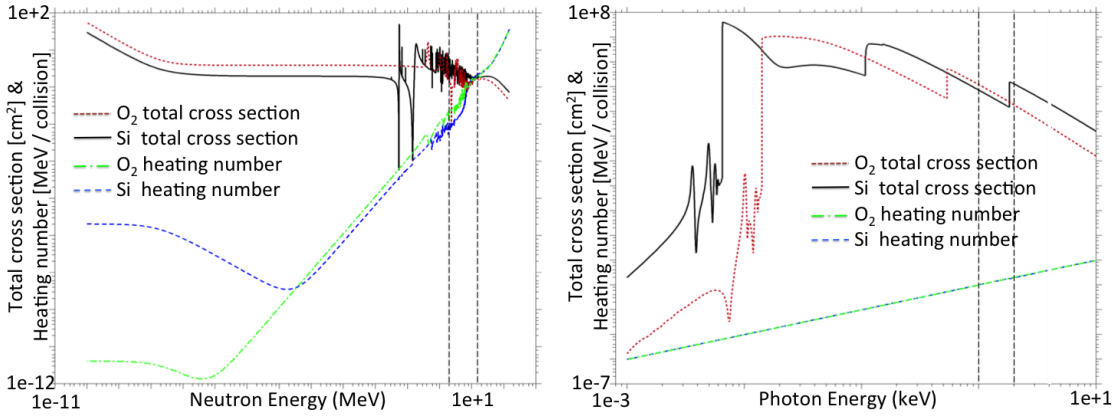

Fig. 1.— MCNP cross sections and heating numbers.

2.2. The RAGE Hydrocode (LANL, *C. Plesko*)

The Radiation Adaptive Grid Eulerian (RAGE) code is the preferred radiation hydrodynamics code in use at Los Alamos National Lab (LANL). RAGE simulations may be carried out in multiple dimensions with a variety of geometries, and with an arbitrary number of constitutive materials via the LANL SESAME database. SESAME is a temperature-based, tabular Equation of State (EOS) library maintained by the Mechanics of Materials and Equations of State group at LANL. The table for each material has an associated unique and thermodynamically consistent fit of semi-empirical theoretical models appropriate to different temperature or pressure regions to experimental data. The majority of SESAME equations of state follow a Mie-Gruenisen model at lower energies and

Thomas-Fermi-Dirac theory at higher energies. Debye theory is used to handle solids, and empirical data are used for phase transitions. Elastic-Plastic and Tepla strength models, Johnson-Cook and Johnson-Holmquist damage models, and P-alpha crush models allow us to model a variety of materials including metals, very porous conglomerates, and brittle geologic materials. The OSO software companys computational geometry design software allows development of detailed, realistic initial conditions. The combination of sophisticated hydrodynamics, gray diffusion radiation transport, and the capacity to handle complicated geometrical structure in a variety of materials makes RAGE promising code for use in modeling asteroid deflection.

2.3. Mercury, Particle Transport Code (LLNL, *R. Managan*)

Mercury can transport neutrons, gamma rays, and light element charged particles using multigroup or continuous energy cross sections. Mercury can perform static and dynamic source calculations; k_{eff} and alpha eigenvalue calculations; and probability of initiation calculations. The code can compute energy deposition and isotopic depletion based on analog or expected value tallies. Tallies, variance reduction, and sources benefit from a wide array of arbitrary user defined fields for very general use capabilities.

Mercury runs efficiently on current generation massively parallel computing platforms and is being improved to enable its use on emerging platforms. Computer science enhancements include dynamically load-balancing parallel calculations, improved methods for visualizing 3-D combinatorial geometries, and implementation of inline visualization capabilities.

Mercury uses the Monte Carlo All Particle Method (MCAPM) library, and data are stored in a pointwise format known as the Evaluated Nuclear Data Library (ENDL). The calculational constants used by Mercury are generated by the MCFGEN processing code to produce MCF files that contain the nuclear data in both multigroup and pointwise forms. Material temperature dependence is added during the processing step. Energy deposits from nuclear reactions are precomputed by a program called ENDEP, which computes the average energy released by the reactions available for each isotope. Thermonuclear reaction rates and secondary particle distributions are provided by the TDF library.

In Mercury, the reactions may be limited to specific subsets of the available reactions. For example, only those reactions that solely produce neutrons or only fission reactions. This keeps the decay chain down to a reasonable set of nuclides for many depletion problems.

2.4. Ares, Hydrodynamics Code (LLNL, *R. Managan*)

Ares is a multi-dimensional, arbitrary Lagrangian/Eulerian (ALE) radiation–hydrodynamics code developed at Lawrence Livermore National Laboratory (LLNL) for applications on massively

parallel computers. This block–structured staggered–mesh code solves the hydrodynamics equations in a Lagrangian coordinate frame. A mesh smoothing and second-order remap scheme is then applied to avoid mesh tangling and associated computational difficulties. Ares can transport radiation with either multi-group diffusion or S_n models. Explicit time integration is accomplished with a second–order predictor–corrector scheme, and spatial differences are computed with a non-dissipative second-order finite element approach. A tensor artificial viscosity is applied for the capturing of shocks and material discontinuities. In addition, the Ares code utilizes adaptive mesh refinement (AMR) to localize computational grid points in regions of interest.

2.5. Spheral, Adaptive Smoothed Particle Hydrodynamics Code (LLNL, *M. Owen*)

Spheral is a mesh-free code intended for modeling hydrodynamics in fluids and solids, and implements a number of meshfree hydrodynamic algorithms. The method utilized in this study is the solids extension of Adaptive Smoothed Particle Hydrodynamics (ASPH: Owen (2010, 2014)). ASPH is a variant of the well known Smoothed Particle Hydrodynamics (SPH: Monaghan (2005)) method modified to allow each point to adapt anisotropically to distortions in the point distribution, something we have found useful for following materials undergoing large deformations (Owen 2014). The ASPH implemenation in Spheral also uses an exactly energy conservative method based on so called "compatible differencing" of the energy equation (Caramana, Burton & Shashkov 1998; Owen et al. 2015), which has been demonstrated to significantly improve the accuracy of (A)SPH models of hypervelocity impacts (Owen et al. 2015). Spheral also employs a tensor generalization of the Benz-Asphaug damage model to follow the failure and fracture of solids (Benz & Asphaug 1994, 1995; Owen 2014), a crucial component in modeling the breakup and ejection of material from an asteroid subjected to either kinetic impactor or energy depostion from a nuclear detonation. Spheral employs a variety of equations of state applicable for hypervelocity material modeling such as the Tillotson (Tillotson 1962), Mie-Gruneisen (Mie 1903; Grüneisen 1912), and the LEOS package from the Livermore equation of state group, as well as a number of strength models. We have applied Spheral to a number of asteroid and planetary modeling efforts (Movshovitz et al. 2015; Owen et al. 1998), and have found it to be well suited to studying the effects of asteroid diversion scenarios.

3. Overview of Test Problems (*K. Howley*)

3.1. Target and Source Input Parameters

We begin by defining the ILTP input parameters for the target asteroid taken from report LLNL-TR-680724. These parameters are summarized in Table 1, left, and the geometry is illustrated in Figure 2. With the exception of asteroid size, the input parameters are identical for the nuclear explosion and kinetic impactor cases. The target asteroid is defined as a spherical object with a 500 m diameter for the nuclear explosion cases, and a 100 m diameter for the kinetic impactor

case. We select target sizes to represent realistic scenarios for which the respective mitigation strategy might be used. For the nuclear cases, a target size comparable to the asteroid 101955 Bennu is selected. Bennu is a 500 m diameter object and the target for the OSIRIS/REx mission (Hergenrother et al. 2014). For the kinetic impactor case, a target size comparable to the secondary in the 65803 Didymos binary system is selected. The secondary, nicknamed "Didymoon", is a 150 m diameter object and, along with the primary, targets for the AIDA mission (ESA 2015). In both mitigation approaches, we define the initial test object as a gray, spherical, non-rotating, monolithic silicon-dioxide (SiO_2) body in hydrostatic equilibrium at an initial temperature of 200 K and a density of 2.65 g/cm^3. For simplicity, the object is characterized as having no strength or porosity.

Table 1: Summary of target asteroid input (left) and source input parameters (right) for ILTP1.

Target Asteroid Input Parameters	
Shape	Spherical
Dynamics	Non-rotating
Diameter	500 m (for **ILTP1n & ILTP1x)**
	100 m (for **ILTP1i)**
Initial Temp	200 K (1.723×10^{-5} keV)
Opacity	Gray
Initial Pressure	In hydrostatic equilibrium
Composition	SiO_2 (^{28}Si, ^{16}O)
Density	2.65 g/cm^3
Porosity	None
Strength	None
EOS:	(1) ANEOS (with a $P_{min} = 0$)
	(2) Mie-Gruneisen[a]
	· $C_0 = 3 \times 10^5$ [cm/s]
	· $S_1 = 1.2$ [unitless]
	· $S_2 = 0$ [unitless]
	· $S_3 = 0$ [unitless]
	· $\gamma_0 = 1.5$ [unitless]
	· b = 0.3 [unitless]

[a]Form from Steinbergs report UCRL-MA-106439

Source Input Parameters	
Source Type	**Stand-off Nuclear Explosion**
Stand-off Dist	100 m
Source Geometry	Point
Pulse Length	0 μs (instantaneous)
Source Yield	(20, 240, 1000) kT
Energy Type	(1) Mono-energetic neutrons (**ILTP1n)**
	(a) 14.1 MeV
	(b) 2.45 MeV
	(2) Planckian x-ray spectra (**ILTP1x)**
	(a) 1 keV
	(b) 2 keV
Source Type	**Kinetic Impactor (ILTP1i)**
Impactor Shape	Sphere
Impact speed	10 km/s
Mass	1 ton
Composition	Al (^{27}Al)
Density	2.7 g/cm^3
Porosity	None
Strength	None
Impactor EOS	Mie-Gruneisen
	· $C_0 = 5.24 \times 10^5$ [cm/s]
	· $S_1 = 1.4$ [unitless]
	· $S_2 = 0$ [unitless]
	· $S_3 = 0$ [unitless]
	· $\gamma_0 = 1.97$ [unitless]
	· b = 0.48 [unitless]

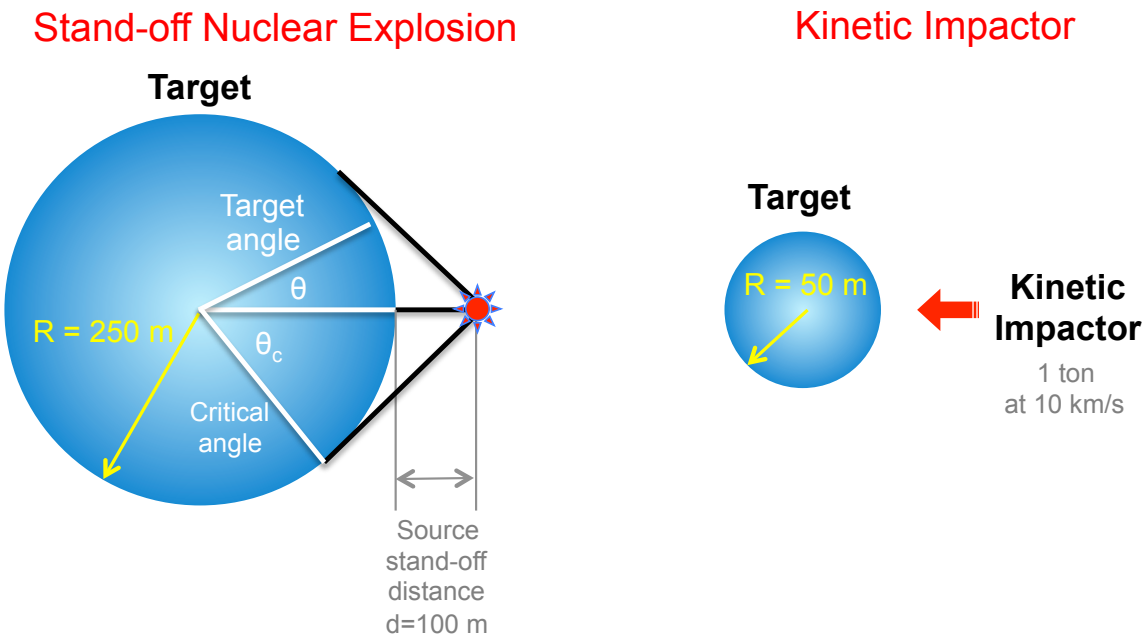

Fig. 2.— Illustration of the setup geometry for ILTP1. On the left, the setup for the stand-off nuclear explosion is shown. On the right, the setup for the kinetic impactor is shown.

Two SiO_2 equations-of-state (EOS) are explored for the test object: (1) a tabular EOS and (2) an analytic Mie Gruneisen. The tabular EOS data is generated using the Analytic Equations of State for Shock Physics (ANEOS, Thompson (1990)) as modified by Melosh (2007). The Mie-Gruneisen EOS parameters, summarized in Table 1, left, are taken from Steinbergs report UCRL-MA-106439.

The neutron and x-ray source parameters used in the stand-off nuclear explosion test problems, ILTP1n and ILTPx, respectively, are summarized in Table 1, top right. The source is modeled as an instantaneous point source at a stand-off distance of 100 m. For the neutron cases, two mono-energetic sources are selected: (1a) a 14.1 MeV source representing the fusion of deuterium and tritium, and (1b) a 2.45 MeV neutron source representing the fusion of two deuterium atoms. For the x-ray cases, two Planckian spectra are selected: (2a) a 1 keV blackbody, and (2b) a 2 keV blackbody. For completeness, a logarithmic range of source yields are chosen for both the neutron and x-ray cases: 20 kT, 240 kT and 1 MT.

The kinetic impactor source parameters are summarized in Table 1, bottom right. The impactor is modeled as an aluminum sphere at a density of 2.7 g/cm^3 using an analytic Mie-Gruneisen EOS. The 1 ton impactor strikes the target normal to the surface at a speed of 10 km/s. For simplicity, the impactor is also characterized as having no strength or porosity.

Table 2: Key metrics and other reportables for ILTP1

Nuclear Deflection	**Key Metric**
(ILTP1n & ILTP1x)	Deflection velocity at 5 ms[b]
	Other Reportables
	Detailed energy deposition approach
	Energy deposition profiles in units of keV/cm^3/kT
	→ As a function of depth at various target angles:
	· 0°, 10°, 20°, 30°, 35°, 40°, 44°
	→ As a function of angle at various target depths:
	· Neutrons: 0cm, 1cm, 10cm , 1m, 10m
	· X-rays: 0cm, 1μm, 10μm, 100μm, 1mm, 1cm, 10cm
	Show time dependence of deflection velocity metric
	Show meshing scheme and resolution
	Demonstrate convergence
	1D planar on-axis results
Kinetic Impactor	**Key Metrics**
(ILTP1i)	Momentum multiplication factor β
	Other Reportables
	Show time dependence of deflection velocity metric
	Show meshing scheme and resolution
	Demonstrate convergence
	Momentum of the center of mass of the asteroid as a function of time

[b]Deflection velocity is defined as z-component of blow-off momentum divided by total (initial) asteroid mass

3.2. Key Metric and Other Reportables

The key metric and other reportables for the stand-off nuclear explosion test problems, ILTP1n and ILTP1x, are summarized in Table 2, top. The key metric is the deflection velocity at 5 ms. This late time is selected to ensure the deflection velocity has asymptoted. The deflection velocity is defined as the z-component of the blow-off momentum divided by the total (initial) asteroid mass. We use this approximation in mass since the blow-off mass is negligible compared to the total asteroid mass. Additional reportables include a detailed overview of the method used to deposit energy into the target, along with the energy deposition profiles as a function of angle and depth. The angular profiles are sampled radially outward every 10° degrees relative to the source-target axis up to 40°, with additional sampling at 35° and 44° to explore the profiles near the limb. For the neutrons, the radial deposition profiles are sampled at the surface and logarithmically inward

from 1 cm to 10 m, and the x-ray deposition profiles are sampled at the surface and logarithmically inward from 1 μm to 10 cm. Since the neutrons have the ability to penetrate more deeply into the target than the x-rays, they are sampled at a coarser radial resolution. To demonstrate that convergence has been achieved, the meshing scheme, resolution and the deflection velocity as a function of time are also to be reported.

The key metric and other reportables for kinetic impactor test problem, ILTP1i, are summarized in Table 2, bottom. The key metric is the momentum multiplication factor β. It is the ratio of the momentum of the ejecta ($p_{\rm ejecta}$) to the momentum of the incoming impactor ($p_{\rm impactor}$) (Housen & Holsapple 2012; Bruck-Syal et al. 2016). The momentum of the asteroid post-impact can be expressed as,

$$\Delta p_{\rm asteroid} = p_{\rm impactor} + p_{\rm ejecta} \quad (2)$$

$$= \beta p_{\rm impactor} \quad (3)$$

where,

$$\beta \equiv 1 + \frac{p_{\rm ejecta}}{p_{\rm impactor}}. \quad (4)$$

Momentum transfer in addition to the incoming impactor momentum can be gained from crater ejecta. Thus, β can take on values greater than one. In addition to the key metric, β, other reportables for ILTP1i include the meshing scheme, resolution and the deflection velocity as a function of time to demonstrate that convergence has been achieved.

4. Stand-off Nuclear Explosion, ILTPn & ILTPx

4.1. MCNP & RAGE Results (LANL, *J. Ferguson*)

It can be seen in Fig. 2 that at a critical angle, θ_c, there is a tangent line from the radiation point source to the asteroid. The revolution of this line generates a cone, and only radiation emitted inside this cone reaches the asteroid. The radiation reaching any surface point, and crossing the surface to enter the asteroid, obviously depends on the emission from the point source and can be written analytically as:

$$F_{sphere}^{enters} = \frac{F_{point}\left[R - (R+d)\cos\theta\right]}{\left[R^2 + (R+d)^2 - 2R\,(R+d)\cos\theta\right]^{3/2}}\,. \quad (5)$$

If the radiation is then assumed to be exponentially attenuated, as it travels through the asteroid, then the radiation flux reaching any point, r, in the asteroid from any surface point, R, is:

$$F_{sphere}^{inside} = F_{sphere}^{enters} e^{-\frac{\|R-r\|}{\lambda}}\,. \quad (6)$$

The radiation deposition from this analytic model is shown in Fig. 3. This analytic model is only meant to verify trends, and provide a minimum of intuition.

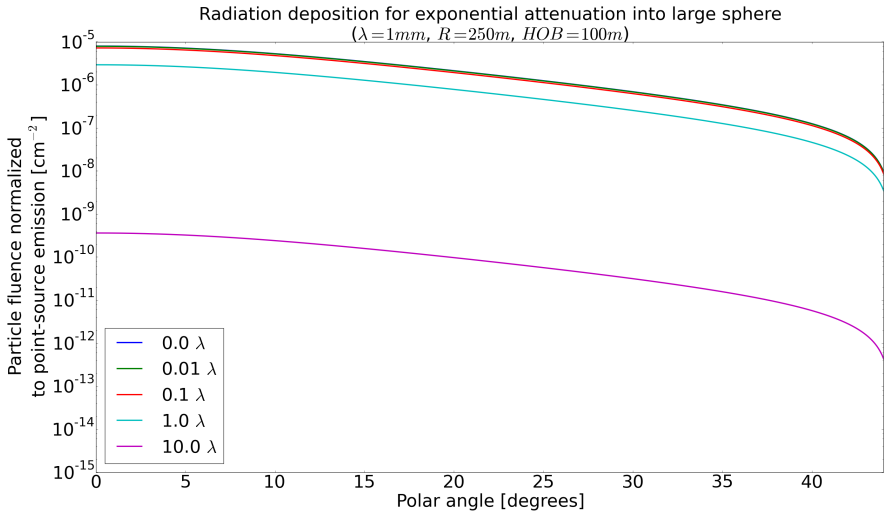

Fig. 3.— (LANL) Analytic exponential attenuation of radiation into the asteroid on a semi-log axis.

Mono-Energetic Neutron Sources (ILTP1n, LANL)

The ILTP1n asks for the neutron angular distributions at depths of [0, 1, 10, 100, 1000] cm, and for the neutron radial distributions along angles of $[0°, 10°, 20°, 30°, 35°, 40°, 45°]$. Figures 4 - 7 present results for the neutron angular and radial distributions. The neutron angular distributions in Figs. 4 and 5 follow similar trends to the analytic exponential attenuation in Fig. 3, but with a few noticeable differences. The first noticeable difference is that the MCNP results show a discontinuity near 35°, and go immediately to 0 at around 37.5°; this will also be seen for the photons, both in MCNP and RAGE. A second distinction from the analytic results for the 2.45 MeV neutrons is that more energy is deposited at 1 cm and 10 cm than closer to the surface (0 cm). This is a boundary layer effect captured by particle transport, i.e., radiation-diffusion solutions will fail to show this effect. Interestingly, the 14.1 MeV neutrons do not show this boundary layer effect at centimeter depths, and instead most of their energy is deposited near the surface and less energy is deposited as the depth is increased.

The neutron radial distributions in Figs. 6 and 7, which are an independent set of MCNP calculations, show similar results to those just mentioned for the 2.45 and 14.1 MeV neutrons, namely that more energy is deposited slightly below the surface for the 2.45 MeV neutrons but not the 14.1 MeV neutrons. It can be seen for the 2.45 MeV neutrons that the energy deposited actually increases with depth along angles 0°, 10°, and even 20°, but not 30° and 35°. However, the 14.1 MeV neutrons do not show this behavior along any angle, nor at any depth greater than 100 μm, which is the smallest depth considered in Fig. 7.

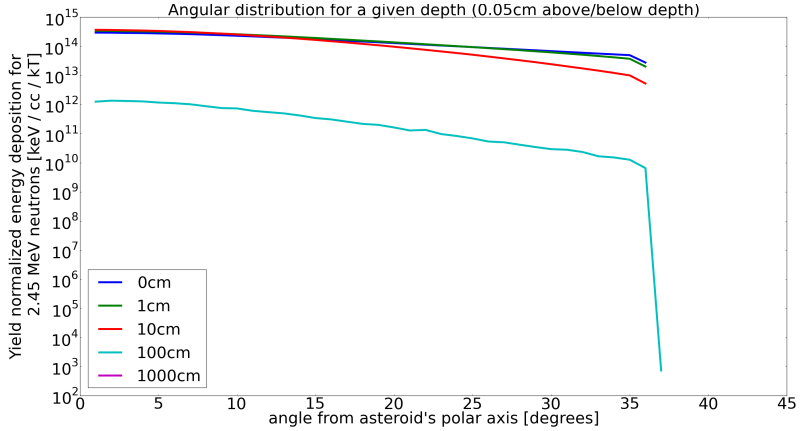

Fig. 4.— (LANL) 2.45 MeV neutron angular distributions at the depths specified in ILTP1n.

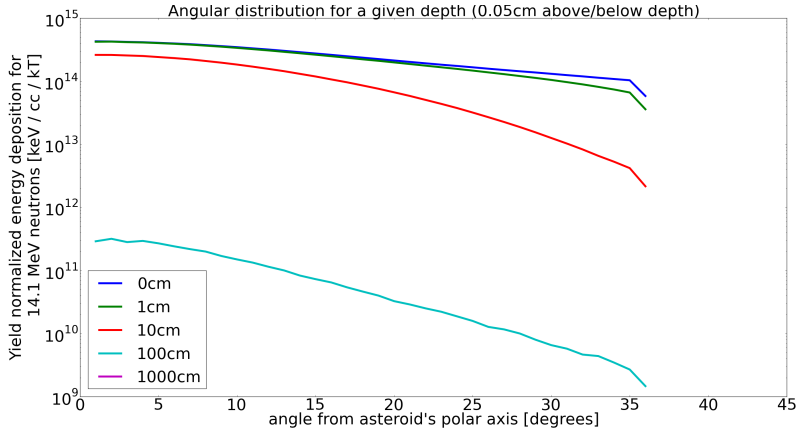

Fig. 5.— (LANL) 14.1 MeV neutron angular distributions at the depths specified in ILTP1n.

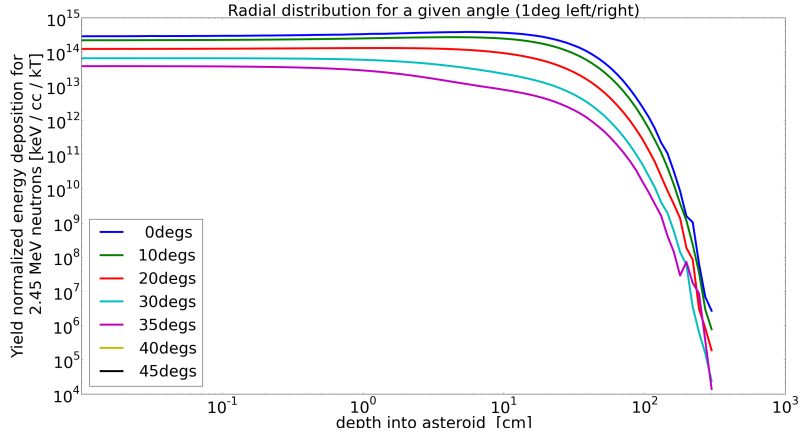

Fig. 6.— (LANL) 2.45 MeV neutron radial distributions along the angles specified in ILTP1n.

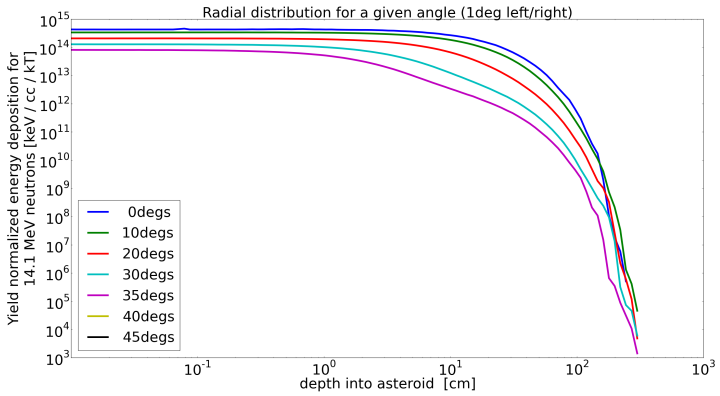

Fig. 7.— (LANL) 14.1 MeV neutron radial distributions along the angles specified in ILTP1n.

We briefly point out that the 2.45 MeV neutrons and the 14.1 MeV neutrons deposit similar amounts of energy into the surface layer of the asteroid, with an effective range between $10^9 - 10^{15}$[keV/cc/kT].

Planckian X-ray Sources (ILTP1x, LANL)

The ILTP1x asks for the photon angular distributions at depths of 0 μm, 1 μm, 10 μm, 100 μm, 1 mm, 1 cm and 10 cm, and for the neutron radial distributions along angles of $0°, 10°, 20°, 30°, 35°, 40°, 45°$. Figs. 8 - 11 present results for the photon angular and radial distributions. Again, the photon angular distributions in Figs. 8 and 9 follow similar trends to the analytic exponential attenuation in Fig. 3, except that, again, the energy deposition presents a discontinuity near 35° and goes to zero near 37.5°. The boundary layer effect, seen for the 2.45 MeV neutrons, is not seen for the photons, neither in Figs. 8 and 9 of the photon angular distributions, nor, more persuasively, in Figs. 10 and 11 of the photon radial distributions. An interesting aspect of their energy deposition profiles is that the 1 keV photons deposit more energy closer to the surface, and less energy at greater depth, than do the 2 keV photons. Depending on the melt and vaporization thresholds of the material, as compared with the energy deposition of the 1 keV and 2 keV photons, this could have interesting consequences for the velocity response of the asteroid. If the melt and vaporization thresholds are in the same vicinity as the energy deposited, perhaps due to the height-of-burst being too high, it is possible that the 1 keV photons will be able to ablate more material from the surface than the 2 keV photons thus pushing the asteroid harder. However, if the melt and vaporization thresholds are far exceeded by both sets of photons it could happen that the 1 keV photons simply overheat the material they ablate, removing substantially less material and not pushing the asteroid as hard. Since the melt and vaporization energies are functions of the material equation-of-state and strength, it is not a straight-forward exercise to compute the asteroid's velocity response from MCNP results alone.

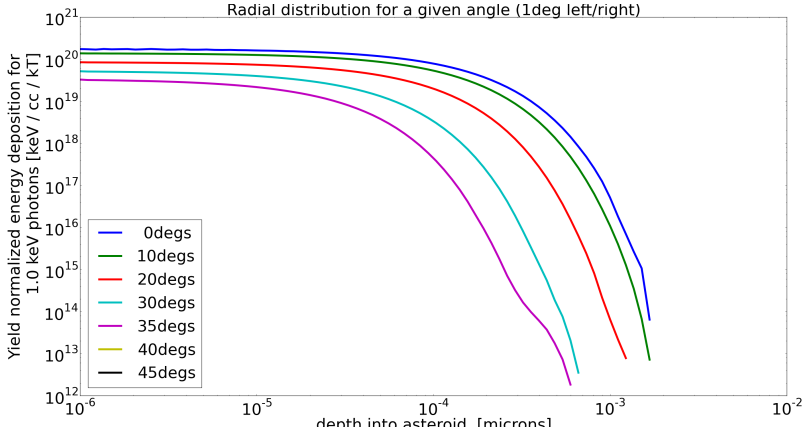

Fig. 8.— (LANL) 1 keV photon angular distributions at the depths specified in the ILTP1x.

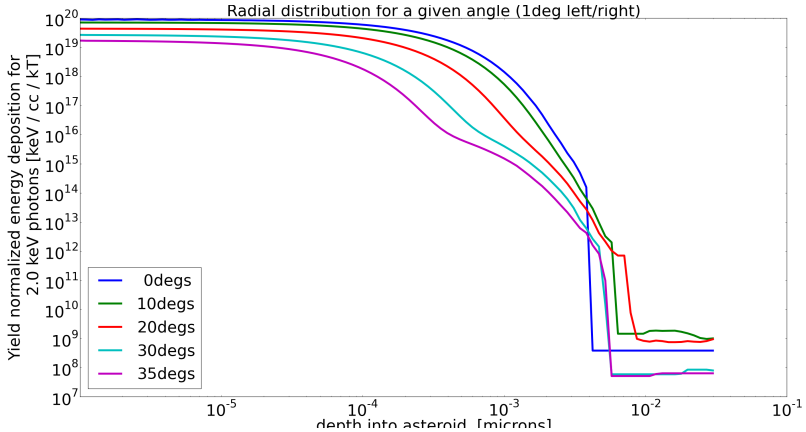

Fig. 9.— (LANL) 2 keV photon angular distributions at the depths specified in the ILTP1x.

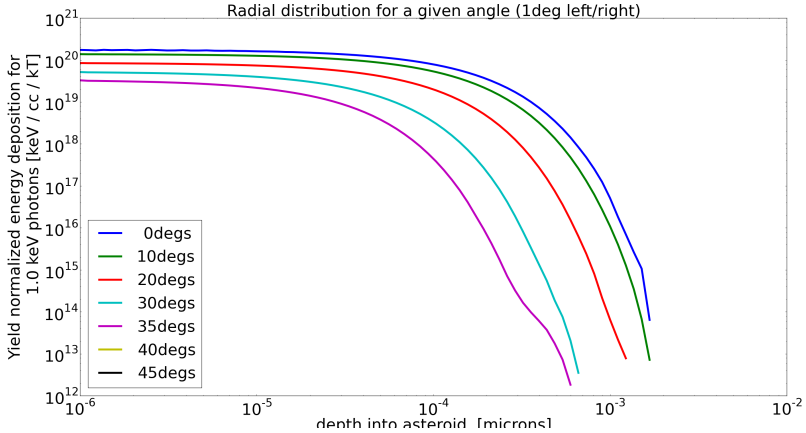

Fig. 10.— (LANL) 1 keV photon radial distributions along the angles specified in the ILTP1x.

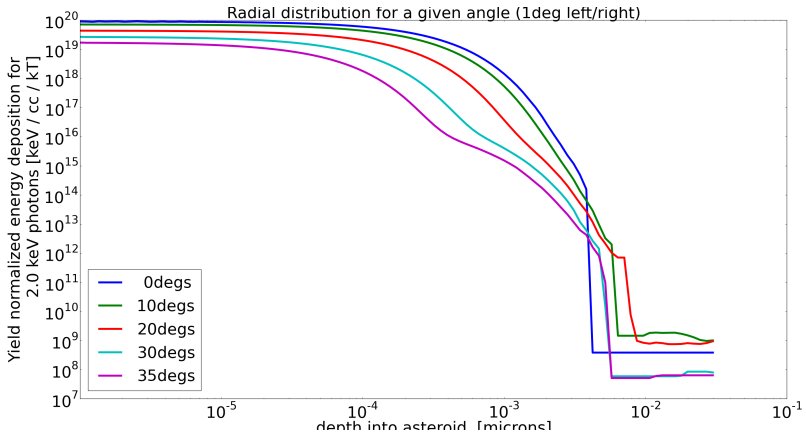

Fig. 11.— (LANL) 2 keV photon radial distributions along the angles specified in the ILTP1x.

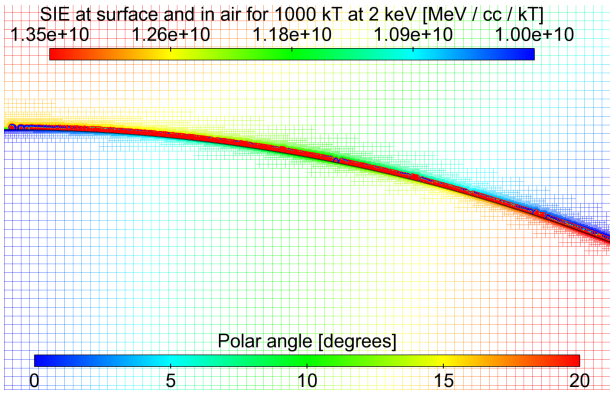

Fig. 12.— (LANL) RAGE meshing at 10 μs for a 2 keV (grey/frequency-independent) 1000 kT radiation source (polyurethane sphere). The largest zones are 128 centimeter squares, and the smallest zones are 1 centimeter squares. Zones much larger than 128 centimeter squares reduce the accuracy of obtaining the desired initial temperature and yield in equilibrium.

To understand the asteroid's velocity response due to the photon's energy deposition we used the Advanced Science Campaign (ASC) radiation-hydrodynamics code, RAGE. In Fig. 12 we present the mesh generally used for these RAGE calculations. The largest zone of the mesh, in the vacuum and inside the asteroid, is a 128 centimeter square, and the smallest zone of the mesh at the interface between the asteroid and the vacuum is 1 centimeter square. When zone sizes larger than 128 centimeter squares are used it becomes harder to ensure that the stand-off radiation source is initialized at the correct temperature and with teh correct amount of energy. Figures 13 and 14 show the angular distribution of energy deposition on the surface of the asteroid for 1 keV and 2 keV grey (frequency-independent) radiation sources with 1000 kT of initial energy (radiation and internal energy, combined). These values are of the order 10^{16} keV/cc/kT in comparison with the

MCNP results above which are of the order 10^{20} keV/cc/kT, which represents 4 orders of magnitude that is not being absorbed by the RAGE asteroid. The reason for this decreased absorption is due to a lack of mesh resolution, which we'll return to shortly. The real purpose of Figs. 13 and 14 is to show that RAGE is generating the correct shape profile, although anomalies do exist near 17.5° and 27.5°, and the energy deposition appears to stop after about 35°. The resultant velocity profiles from RAGE, for four sources, 1000 kT at 1 keV and 2 keV, as well as 20 kT and 240 kT at 2 keV, are presented in Fig. 15. It is no surprise that the 1000 kT sources at both 1 keV and 2 keV dominate the velocity responses of the other two radiation sources. Returning to the lack of mesh resolution, Fig. 16 shows the effect of the mesh resolution on the asteroid's ablation velocity. The difference between 10 centimeter square zoning and 1 centimeter square zoning is approximately a factor of 6.5 in ablation velocity. Lack of mesh resolution is the single largest reason the RAGE velocity response predictions are considerably lower than those from LLNL.

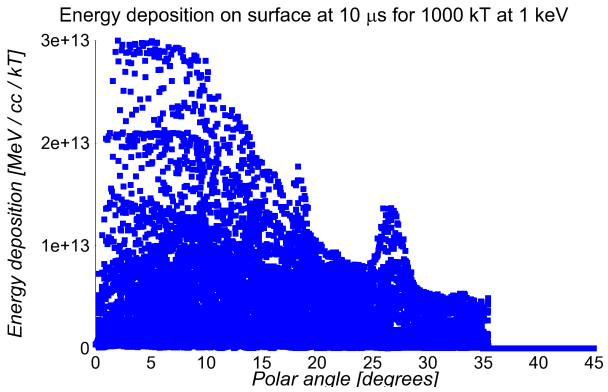

Fig. 13.— (LANL) RAGE energy deposition at the surface of the asteroid for a 1 keV (grey/frequency-independent) 1000 kT radiation source (polyurethane sphere).

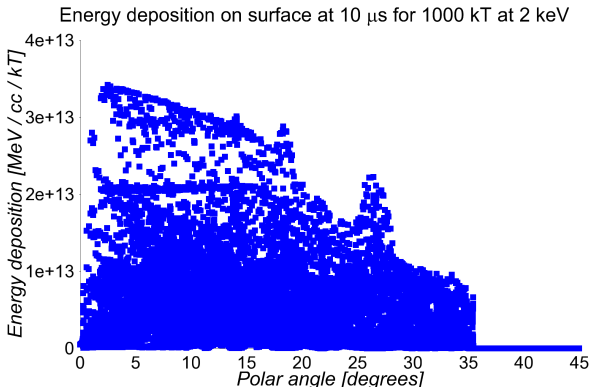

Fig. 14.— (LANL) RAGE energy deposition at the surface of the asteroid for a 2 keV (grey/frequency-independent) 1000 kT radiation source (polyurethane sphere).

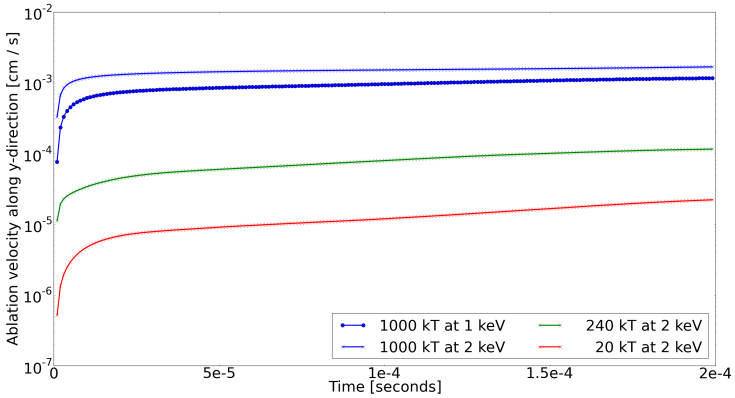

Fig. 15.— (LANL) Velocity response profiles.

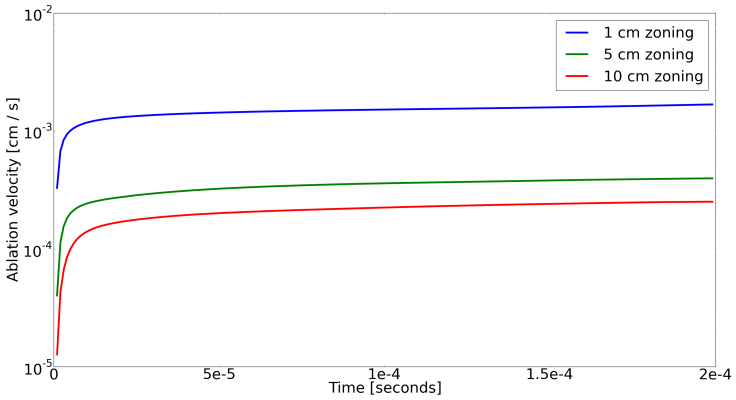

Fig. 16.— (LANL) Velocity response profiles.

4.2. Mercury & Ares Results (LLNL, *K. Howley*, *R. Managan*, *J. Wasem*)

One-dimensional (1D) energy deposition profiles into SiO_2 for each energy type are modeled using the particle transport code, Mercury (see § 2.3). These profiles are fit with an exponential function to construct an analytic approximation of the energy coupling using Howley, Managan & Wasem (2014),

$$\epsilon_{dep}(r) = \epsilon_0 \exp\left(-\frac{R-r}{\lambda_d}\right), \tag{7}$$

where where ϵ_0 is the deposited energy density at the surface, R is the radius of the target, $R-r$ is the depth relative to the target surface, and λ_d is the skin depth for the corresponding energy type. These profiles are then scaled with source yield [20, 240, 1000] kT and mapped onto a two-dimensional (2D) hydrodynamic mesh for simulation in Ares (see § 2.4). Only material that has been melted or vaporized and ejected with a velocity above escape velocity will contributed to the blowoff momentum. Using Howley, Managan & Wasem (2014) the depth of material melted can be approximated analytically,

$$z_{\rm melt} = \lambda_d \ln \frac{\epsilon_0}{\epsilon_{\rm melt}}, \tag{8}$$

where $z_{\rm melt}$ is the depth of material melted and $\epsilon_{\rm melt}$ is the melt energy density for SiO_2 $\sim$ 5.1 kJ/cm^3 (Richet & Bottinga 1988). We use the ANEOS equation of state to model the material response, which has a melt energy density consistent with the experimentally determined values. To ensure adequate resolution of the hydrodynamic mesh, resolutions in accordance with Howley, Managan & Wasem (2014) are selected such that the errors introduced into the blow-off momentum are less than 10%,

$$\%\text{Error} \approx 22.8\frac{\Delta r}{z_{\rm melt}}, \tag{9}$$

where Δr is the resolution needed to a depth $z_{\rm melt}$ (Howley, Managan & Wasem 2014).

Mono-Energetic Neutron Sources (ILTP1n, LLNL) The simulated deflection velocities for the 2.45 MeV neutron sources are as follows: 6.7 cm s^{-1} at 1 MT, 1.0 cm s^{-1} at 240 kt and 0 cm s^{-1} at 20 kt. The simulated deflection velocities for the 14.1 MeV neutron sources are 4.0 cm s^{-1} at 1 MT, 0.6 cm s^{-1} at 240 kT and 0 cm s^{-1} at 20 kT. The reason that no deflection occurs in the 20 kT cases is because energy from the incoming neutrons goes into heating the material, but not melting it, and, as a result, no mass is ejected. These results are summarized in Table 3. The time dependence of the deflection velocity for each of the neutron cases is shown in Figure 17. Convergence in time of the deflection velocity is demonstrated for the neutron sources.

The Mercury particle transport code was used to determine the deposition profiles for the 2.45 MeV neutrons and the 14.1 MeV neutrons into SiO_2 at a density of 2.65 g/cm^3. The analytic approximations to these energy deposition profiles at angles of 0°, 10°, 20°, 30°, 35°, 40° and 44° relative to the asteroid center, and at depths of 0 cm, 1 cm, 10 cm, 1 m and 10 m from the asteroid surface are shown in Figures 18 and 19. For the 2.45 MeV neutron cases, 21% of the source yield is deposited in the target. For the 14.1 MeV neutron cases 11% of the source yield is deposited. The reason for this difference is the yield coupling efficiency of the material, a 2.45 MeV neutrons deposits a larger fraction of its energy into SiO_2 than a 14.1 MeV neutron. The depths of material melted on axis ($\theta = 0°$) for the 2.45 MeV neutron cases are as follows: 144 cm at 1 MT, 80 cm at 240 kT, and no material melted at 20 kT. For the 14.1 MeV neutrons the depths of material melted on axis ($\theta = 0°$) are 64 cm at 1 MT, 35 cm at 240 kT, and no material melted at 20 kT. The

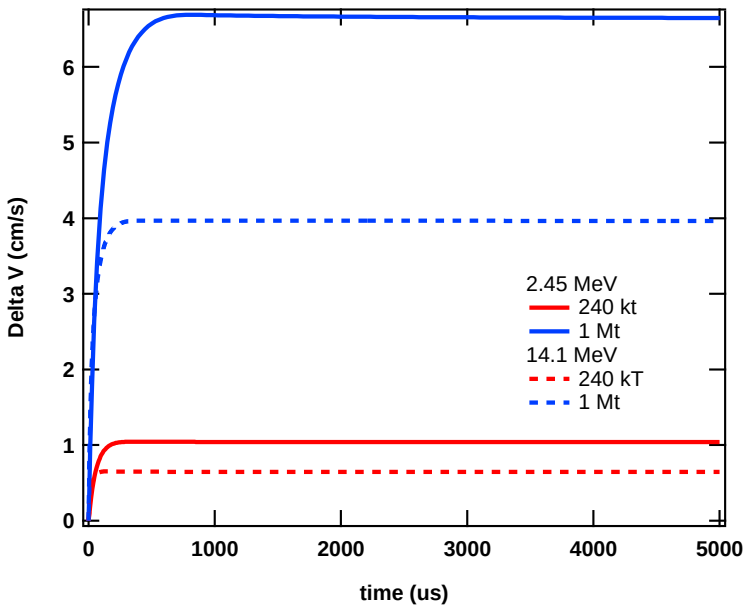

Fig. 17.— (LLNL) Time dependence of the target's deflection velocity for the stand-off neutron source cases. In blue are the 1 MT sources, and in red are the 240 kT sources. The solid lines denote the 2.45 MeV neutron sources, and the dashed lines denote the 14.1 MeV sources.

Table 3: (LLNL) Summary of Mercury & Ares Results for the stand-off nuclear explosion test problems, ILTP1n & ILTP1x

Source Energy Type		Source Yield (kT)	Stand-off Distance (m)	Radiation Fraction[c]	Effective Energy Deposited (kT)	Resolution[c]	On-Axis ($\theta = 0°$) Melt Depth	Deflection Velocity (cm/s)
Neutrons	2.45 MeV	1000	100	0%	207	4.0 cm	144 cm	**6.7**
		240			50	0.8 cm	80 cm	**1.0**
		20[e]			4.1	-	-	-
	14.1 MeV	1000		0%	108	0.2 cm	64 cm	**4.0**
		240			26	0.75 cm	35 cm	**0.6**
		20[e]			2.2	-	-	-
X-Rays	1 keV	1000		∼ 80%	30	0.4 μm	140 μm	**0.080**
		240			7.2	0.4 μm	120 μm	**0.036**
		20			2.4	0.2 μm	0.6 μm	**0.009**
	2 keV	1000		∼ 80%	30	2 μm	800 μm	**0.241**
		240			7.2	2 μm	700 μm	**0.083**
		20			0.6	1 μm	500 μm	**0.015**

[c]Fraction of energy deposited energy radiated away from the surface prior to hydrodynamic motion

[d]Hydro resolution needed to constrain deflection velocity errors to $\leq 10\%$ (Howley, Managan & Wasem 2014)

[e]We determine that the 20 kT neutron cases do not reach temperatures high enough to melt material, and therefore to not produce any appreciable deflection

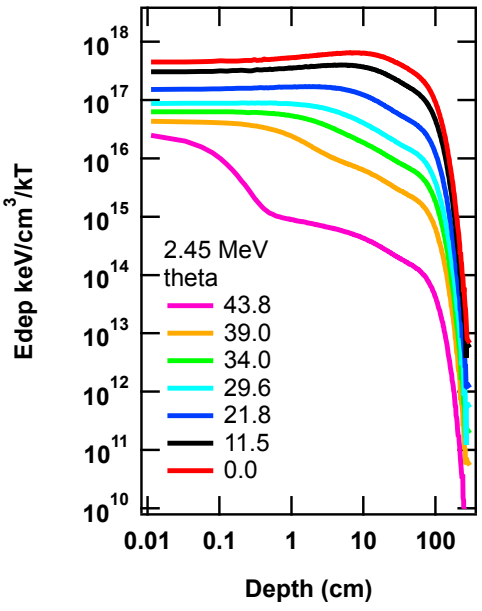

Fig. 18.— (LLNL) Mercury energy deposition profile for 2.45 MeV neutrons into SiO_2 as a function of depth and angle.

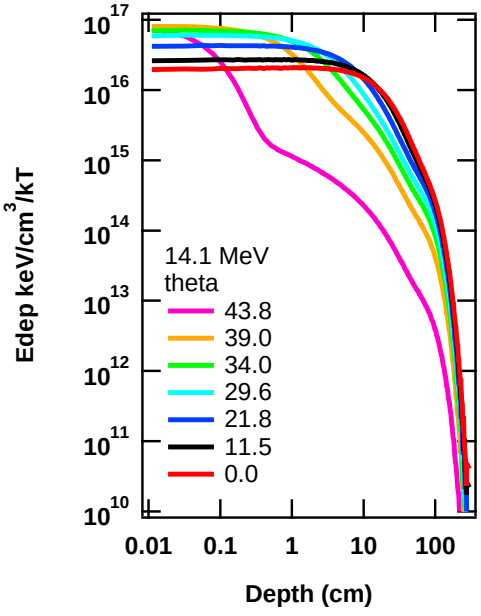

Fig. 19.— (LLNL) Mercury energy deposition profile for 14.1 MeV neutrons into SiO_2 as a function of depth and angle.

analytic melt depths are in agreement with the melt depths measured in the simulations. Using Equation 9, the resolution needed to resolve the deflection velocity to within 10% near the limbs of the body is determined. For the 2.45 MeV neutrons the zone size needed down to the on-axis melt depth is 4 cm at 1 MT, and 0.8 cm at 240 kT. For the 14.1 MeV neutrons the zone size needed down to the on-axis melt depth is 0.2 cm at 1 MT, and 0.75 cm at 240 kT.

Planckian X-ray Sources (ILTP1x, LLNL) The simulated deflection velocities for the 1 keV Planckian distributed x-ray sources are as follows: 0.080 cm s^{-1} at 1 MT, 0.036 cm s^{-1} at 240 kt and 0.009 cm s^{-1} at 20 kt. The simulated deflection velocities for the 2 keV Planckian distributed x-ray sources are 0.241 cm s^{-1} at 1 MT, 0.083 cm s^{-1} at 240 kT and 0.015 cm s^{-1} at 20 kT. These results are summarized in Table 3. The time dependence of the deflection velocity for each of the x-ray cases is shown in Figure 20. For the 2 keV Planckian distributed x-rays convergence in time of the deflection velocity is demonstrated for at 20 kT, and near convergence is demonstrated at 240 kT and 1 MT. Convergence was not reached for the 1 keV Planckian distributed x-rays, likely because the required mesh resolution results in tiny simulation time steps.

The Mercury particle transport code was used to determine the deposition profiles for the 1 keV and 2 keV Planckian distributed x-rays into SiO_2 at a density of 2.65 g/cm^3. The analytic approximations to these energy deposition profiles at angles of 0°, 10°, 20°, 30°, 35°, 40° and 44° relative to the asteroid center, and as a function of depth from the asteroid surface are shown in

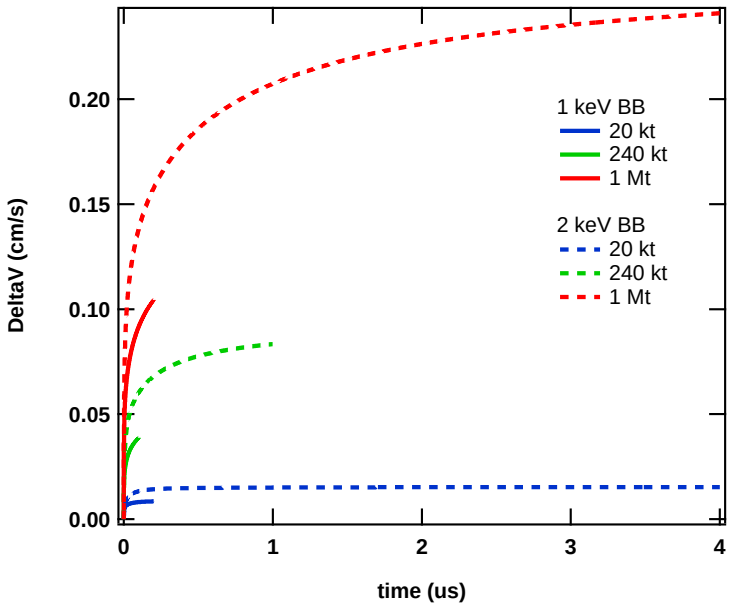

Fig. 20.— (LLNL) Time dependence of the target's deflection velocity for the stand-off x-ray source cases. In blue are the 1 MT sources, red are the 240 kT sources, and orange are the 20 kT sources. The solid lines denote the 1 keV Planckian distributed x-ray sources, and the dashed lines denote the 2 keV Planckian distributed x-ray sources.

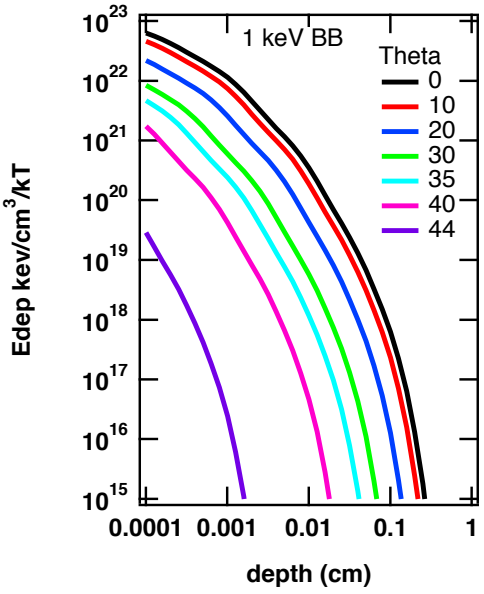

Fig. 21.— (LLNL) Mercury energy deposition profile for 1 keV Planckian distributed x-rays into SiO_2 as a function of depth and angle.

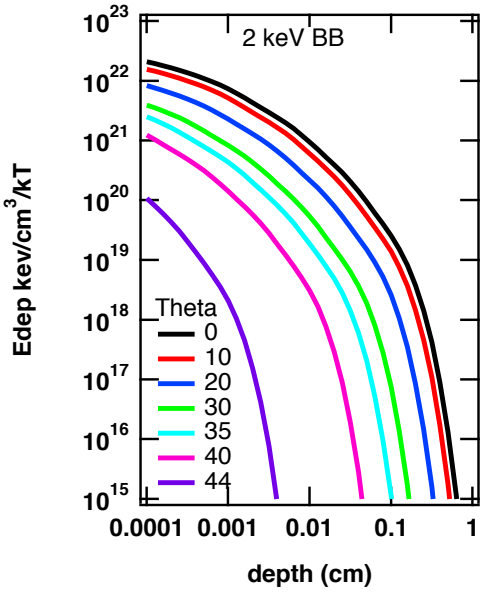

Fig. 22.— (LLNL) Mercury energy deposition profile for 2 keV Planckian distributed x-rays into SiO_2 as a function of depth and angle.

Figures 21 and 22. For both cases, 15% of the source yield is deposited into the target. However, of this deposited yield, 80% is radiated away prior to hydrodynamic motion. This is because during the radiation deposition phase of a nuclear deflection attempt, these x-rays deposit the majority of their energy very close to the asteroid surface. This results in the material temperature becoming highly elevated, to the point where the material itself will blackbody radiate back into space at a significant rate. At high enough temperatures this re-radiation can remove a very large fraction of the originally deposited energy, and do so on timescales that are noticeably less than the characteristic hydrodynamic timescale for the material response. We thus approximate, to a high degree of accuracy, the re-radiation phase as a process that occurs following the original deposition but prior to any material motion. While details of the deflection attempt (yield, stand-off distance, output spectrum, asteroid material type, etc.) affect the final fraction that is re-radiated, a nominal figure for this fraction for 1 to 2 keV blackbody incident radiation is 80%, meaning that of the energy originally intercepted and absorbed by the asteroid only approximately 1/5th will remain in the asteroid to affect blowoff momentum following the re-radiation phase.

The hydrodynamic resolution needed to produced deflection velocities to within 10% and depths of material melted are determined over the range of test problem yields for the 1 keV and 2 keV Planckian distributed x-ray cases. The depths of material melted on axis ($\theta = 0°$) for the 1 keV Planckian distributed x-ray cases are as follows: 140 μm at 1 MT, 120 μm at 240 kT, and 89 μm at 20 kT. For the 2 keV Planckian distributed x-ray cases the depths of material melted on

axis ($\theta = 0°$) are 800 μm at 1 MT, 700 μm at 240 kT, and 500 μm at 20 kT. The analytic melt depths are in agreement with the melt depths measured in the simulations. Unlike the neutron cases, material *is* melted at source yields of 20 kT. This is because x-ray energy is deposited over a significantly shallower depth than the neutron energy resulting in a higher material temperature near the surface. Using Equation 9, the resolution needed to resolve the deflection velocity to within 10% near the limbs of the body is determined. For the 1 keV Planckian distributed x-ray cases the zone size needed down to the on-axis melt depth is 0.4 μm at both 1 MT and 240 kT, and 0.2 μm at 20 kT. For the 2 keV Planckian distributed x-ray cases the zone size needed down to the on-axis melt depth is 2 μm at both 1 MT and 240 kT, and 1 μm at 20 kT.

4.3. Conclusions for ILTP1n & ILTP1x Code-to-Code Comparison (*J. Ferguson*, *K. Howley*, *R. Managan*, *J. Wasem*)

For this work a comparison was made over two different classes of radiation (x-rays and neutrons) at two different energies each, in two different temporal regimes (initial radiation deposition and subsequent hydrodynamic response). Beginning with the neutron radiation deposition phase, the deposition profiles achieved by both the LANL MCNP work and the LLNL Mercury results were largely in agreement with respect to both depth of penetration as well as the energy density achieved. As noted by both laboratories, the on-axis results (those near 0 degrees angle of incidence) for the 2.45 MeV neutrons exhibit the behavior that the deposited energy density increases slightly between 1 and 10 cm depth. This behavior is not seen with the 14.1 MeV neutrons (nor with the x-rays, as shown below in Figures 25 and 26), and is perhaps counter-intuitive to what one might expect to be a monotonically decreasing deposition profile. This has been shown to be due to the presence of energy-enhancing n-gamma interactions with the Si-28 in the asteroid, which occur primarily for 2.45 MeV neutrons, but not for 14.1 MeV neutrons and not for x-rays.

For the neutron hydrodynamic response phase, the deposition profiles calculated by both labs indicate that the surface resolution needed to adequately capture the spatial variation of the energy is around 1 cm or less. This is borne out by the results from LLNL shown in Table 3. Resolutions lower than this will give unconverged results, and in pathologically under-resolved cases will result in potentially no deflection at all. Examining the results in Table 3 further, one can see that (as expected) a larger source yield achieves a higher deflection velocity, and that for the stand-off distances and yields involved, the neutron sources will give multi-centimeter per second deflections. Also, the lowest yield of 20 kT did not result in a deflection at all. This is an exhibition of the "microwave effect" where the energy deposited is distributed over a large enough area such that the material does not achieve melt or vaporization, and therefore does not contribute to deflection. The physics behind this effect is very important to get right, and is intimately tied to the need for adequate spatial resolution in the hydrodynamic simulation, as discussed above. For further discussion of this effect, the reader should look at Howley, Managan & Wasem (2014).

Moving now to a comparison of the x-ray deposition phase the results reported by the two

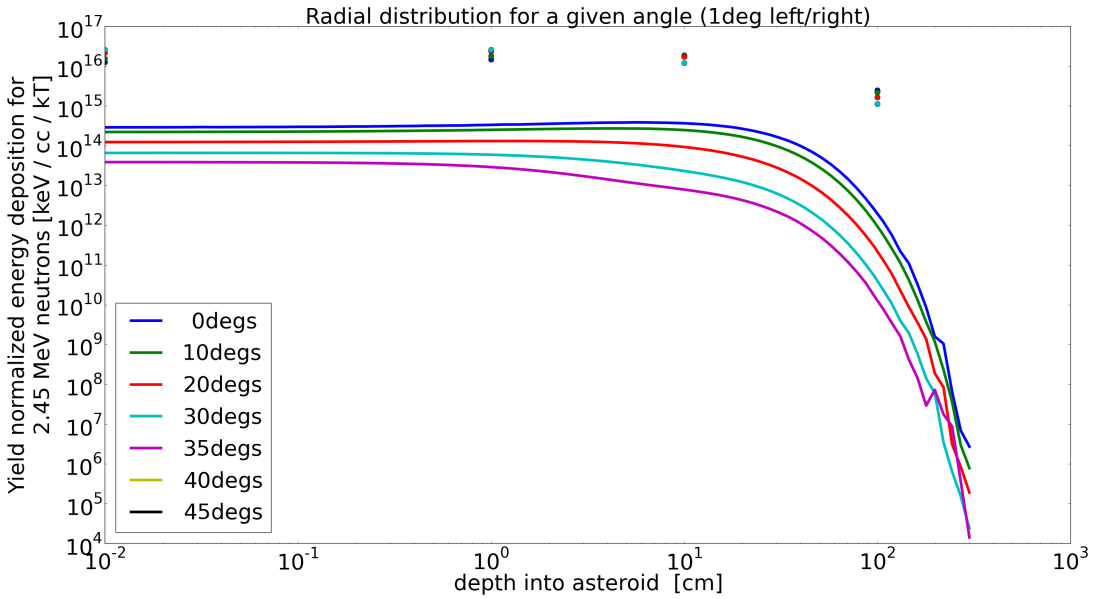

Fig. 23.— Comparison of MCNP (solid lines) and Mercury's (circles) energy deposition profiles for 2.45 MeV mono-energetic neutrons. Colors denote profiles as a function of angle.

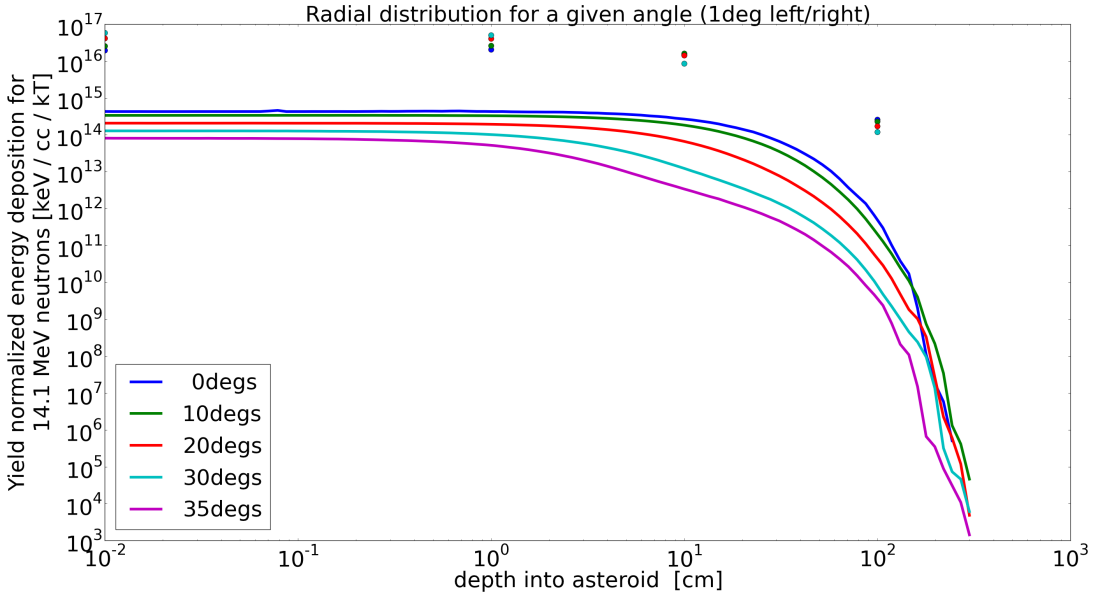

Fig. 24.— Comparison of MCNP (solid lines) and Mercury's (circles) energy deposition profiles for 14.1 MeV mono-energetic neutrons. Colors denote profiles as a function of angle.

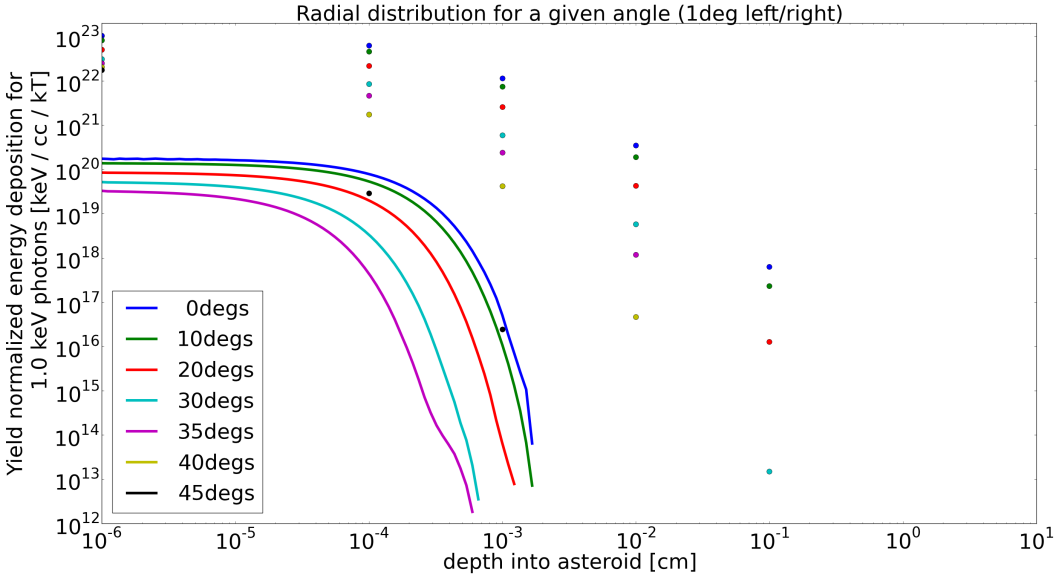

Fig. 25.— Comparison of MCNP's energy deposition profiles for monoenergetic 1 keV x-rays (solid lines) and Mercury's energy deposition profiles for 1 keV Planckian distributed x-rays (circles). Colors denote profiles as a function of angle.

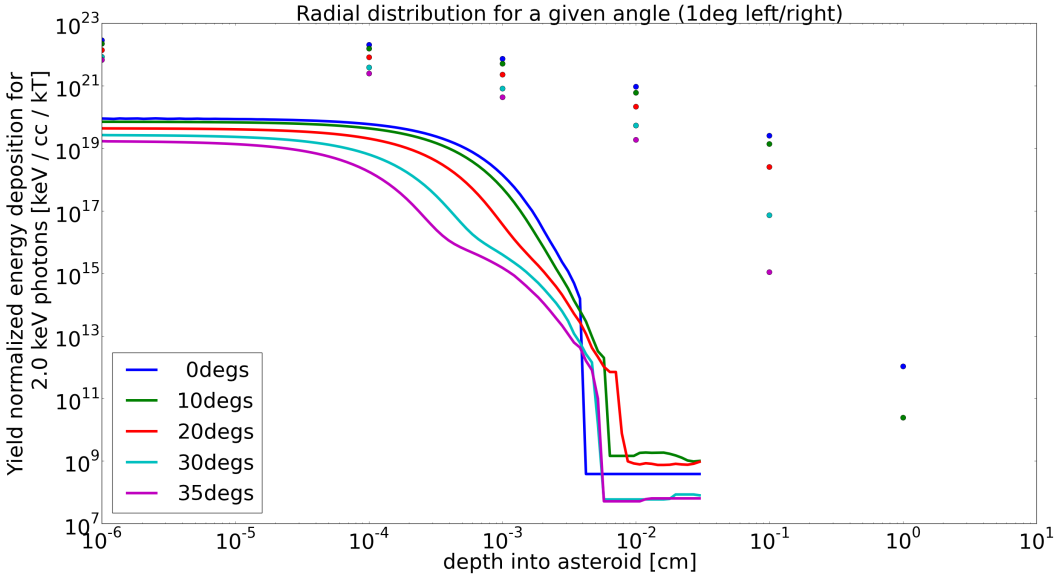

Fig. 26.— Comparison of MCNP's energy deposition profiles for monoenergetic 2 keV x-rays (solid lines) and Mercury's energy deposition profiles for 2 keV Planckian distributed x-rays (circles). Colors denote profiles as a function of angle.

labs are in good qualitative agreement, but have noticeable quantitative differences. This is due to slightly different problem definitions used by each lab. For its results LLNL used 1 and 2 keV Planckian sources, while LANL used 1 and 2 keV monochromatic sources. A blackbody distribution for a given temperature T will have a peak in it's x-ray spectrum at approximately $3\,T$, with exponentially falling contributions to x-rays at energies above and below that number. Thus a 1 keV Planckian will have a spectral peak at 3 keV in the x-ray energy, with contributions at energies around that value. A 1 keV monochromatic source, by contrast, will only contain 1 keV x-rays. Thus, the spectrum used by LLNL contains x-rays with noticeably higher energies that the LANL spectrum, leading to larger penetration depths and a different deposition profile.

The deposition profiles for both the LLNL and LANL input spectra indicate that for the hydrodynamic response phase of the calculation a resolution on the order of microns is necessary to correctly represent the energy distribution deposited by the x-rays. This allows for a few zones in the hydrodynamic simulation to achieve the very high temperatures that the surface of the asteroid would during a deflection attempt. Thus, sufficient zoning in the problem will allow a few near-surface zones to be very hot, while zones even only a centimeter into the asteroid may initially only attain a modest temperature. Among other effects observed, this will lead to substantial re-radiation, as described in the section above, as well as a few surface zones that move at very high velocity and contribute the majority of the momentum change despite representing a small mass fraction.

Conversely, zoning that is too large will result in significantly lower momentum changes and/or the "microwave effect" described above. However, higher resolution zoning also requires a significant increase in computational memory and speed to handle the higher resolved problem. This was found to be a significant impediment for the Rage code, where minimum zone sizes of 1 cm were found to be the highest resolution computationally achievable. In the code Ares, a different approach was taken where the problem had small (sub-micron) material zoning near the surface and then gradually increased the zone size as one went deeper into the asteroid. This resulted in a smaller overall problem size (fewer total zones) as well as high resolution zoning near the surface where the x-ray deposition length was important. It is believed that the difference in zoning techniques makes up the bulk of the difference in deflection velocities observed in the data above. For this reason it is now believed that for appropriate meshing a Lagrangian code would be preferable.

While the majority of the difference observed in deflection velocities is due to zoning issues there are several other substantial differences between the Rage and Ares calculations of the hydrodynamic responses using x-rays. The Ares runs used input from the Mercury deposition profile which utilized a constant temperature Planckian source with a given total energy. This deposition was then cut by 80% to account for re-radiation effects and the energy per unit mass remaining sourced into an Ares hydrodynamic calculation. This achieves correct transport results for the x-rays from the source to the asteroid and results in the correct final deposition profile, but makes the approximation that the deposition and hydrodynamic timescales are well separated.

In contrast, the Rage runs uses a polyurethane ball of variable radius with sourced energy per unit mass to achieve both the correct total yield and initial temperature. The radiation from this hot ball then is allowed to diffuse through a vacuum to the asteroid and deposit its radiation energy, using a very low-density gas and the grey diffusion radiation approximation. This approximation is not a constant temperature source, but rather a Planckian source that is allowed to cool, leading to an average spectrum that is softer. The diffusion approximation also tends to allow the radiation to flow somewhat around the asteroid as it penetrates, leading to a wider "footprint" on the surface. However, in the Rage calculations there is no assumption of split deposition and hydrodynamic timescales. Re-radiation occurs naturally in this problem setup, but as noted earlier it is highly sensitive to zoning and as such it is likely that with 1 cm zones there is effectively no re-radiation being accounted for. While it is believed that these differences are small compared to the zoning differences discussed earlier, it is likely that they would result in non-negligible quantitative differences themselves.

5. Kinetic Impactor, ILTP1i

5.1. RAGE Results (LANL, *G. Gisler*)

Using the Los Alamos RAGE hydrocode Gittings et al. (2009) described in Section 2.2, we perform a series of calculations to study the dependence of β on the composition, strength, and porosity of the asteroid, given a projectile of specified mass and impact speed. For strength we have used both Steinberg-Guinan and Wilkins-Gittings models. For equations of state we have used LANL SESAME tables and analytic Mie-Grneisen formulas. Both the projectile and the asteroid are immersed in, and in thermal and pressure equilibrium with, a low-pressure (100 microbar) ideal monatomic gas. RAGE cannot run with a background vacuum. RAGE uses cell-by-cell adaptive mesh refinement to give high accuracy in regions of the problem where it is most needed, for example at the interface between the projectile and the asteroid during the cratering process. In these runs we use a finest resolution of 0.3125 cm during the initial phases, gradually relaxing that during the course of the calculation for computational efficiency in the later stages when the ejecta

Table 4: (LANL) Results for RAGE Hydrocode Models of a Kinetic Impactor

Model	Code	r (m)	Porosity	ρ (g/cc)	M_{proj} (kg)	v_{proj} (km/s)	β_t	β_m
eD12	RAGE	100	0	2.65	1086	10	31	31
eD14	RAGE	100	0.17	2.21	1086	10	4.63	7.13
eD16	RAGE	100	0.38	1.66	1086	10	2.18	3.73
eD18	RAGE	100	0.50	1.33	1086	10	1.83	2.88
eD19	RAGE	100	0.55	1.20	1086	10	1.62	1.86

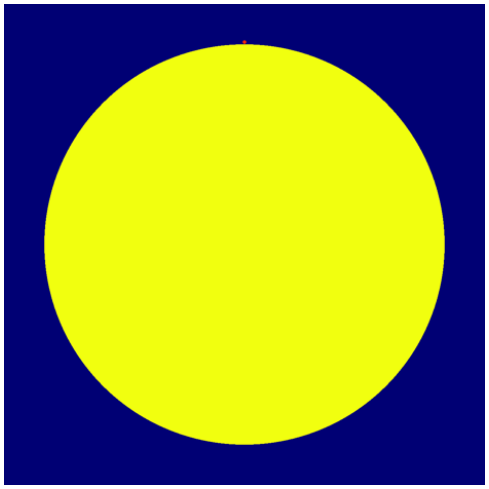

Fig. 27.— (LANL) Configuration space plot of the initial condition of a typical kinetic-impact run. The asteroid in yellow is 100 m in diameter, and the tiny red dot above is the impactor 92 cm in diameter, massing 1.09 metric ton. The calculation is axisymmetric about the line of impact, but the axial direction is referred to as y. The projectile thus has a negative y velocity.

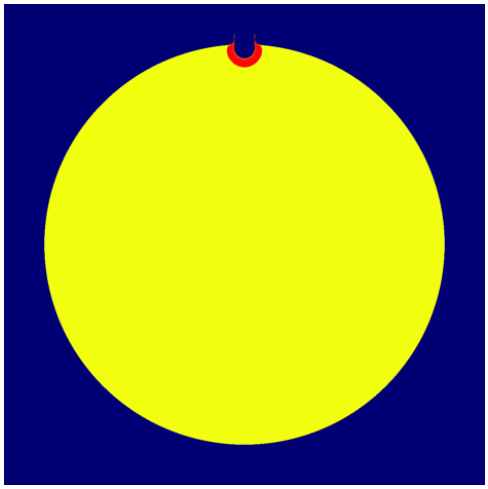

Fig. 28.— (LANL) Configuration-space plot of the asteroid 3 ms after impact, colored by density. A small impact crater is already formed at the impact point, and ejecta are beginning to stream upward, in the positive y direction.

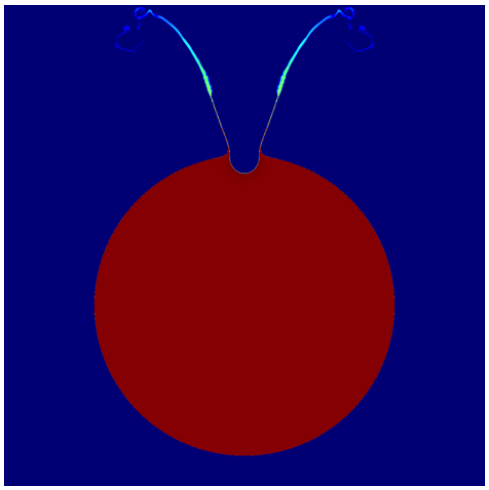

Fig. 29.— (LANL) Configuration-space log-density plot of the asteroid and its ejecta at 0.02 seconds after impact.

are simply expanding away from the bulk of the asteroid. The initial condition for run eD14 (see Table 4) is illustrated in Figure 27. Figure 28 shows the impact crater at 3×10^{-3} seconds later, in the same run, and Figure 29 shows the impact crater and ejecta at 2×10^{-2} seconds later, zoomed out and with a logarithmic density scale.

Analysis of the efficiency of the transfer of momentum from the projectile to the asteroid was performed in two different ways. In one method, 946 massless Lagrangian tracers were distributed uniformly throughout the body of the asteroid. The tracers register the physical conditions at their locations, and move with the velocities in the cells in which they reside. Those that achieve escape velocity from the asteroid (calculated from the asteroid's initial mass and radius), sit on or outside the asteroid surface, and have an outward directed velocity, are regarded as ejected. Most ejecta come from the vicinity of the crater, with positive $\hat{y}$ velocities (the projectile has $-\hat{y}$ velocity), and augment the momentum transferred to the remainder of the asteroid. An example calculation using this method is shown in Figure 30.

In the second method, the entire calculational domain is inspected for fractional masses of

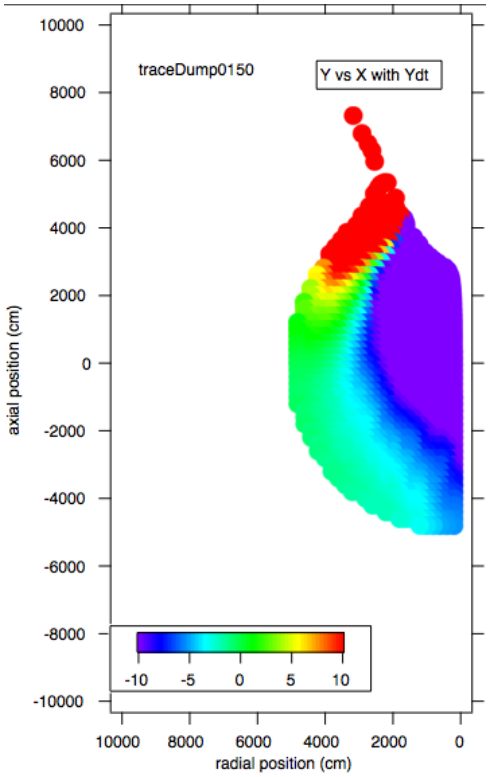

Fig. 30.— (LANL) Configuration-space plot of tracer positions, colored by axial velocity, in run eD18 at time 0.15 seconds after impact. Escape velocity from the asteroid is 4.3 cm/s, so many of the red-colored tracers (those on or away from the surface) are or will be ejecta.

asteroid, projectile, and background material, and tallies are made of mass and momenta of each material. As with the tracers, asteroid material that is on the surface with an outward directed velocity greater than needed for escape is considered ejected. This method has the advantage that the exchange of momentum from the projectile to the asteroid can be directly monitored, and the contribution of nonphysical background contribution to the momentum exchange can be controlled. An illustration of this is shown in Figure 31 for run eD18.

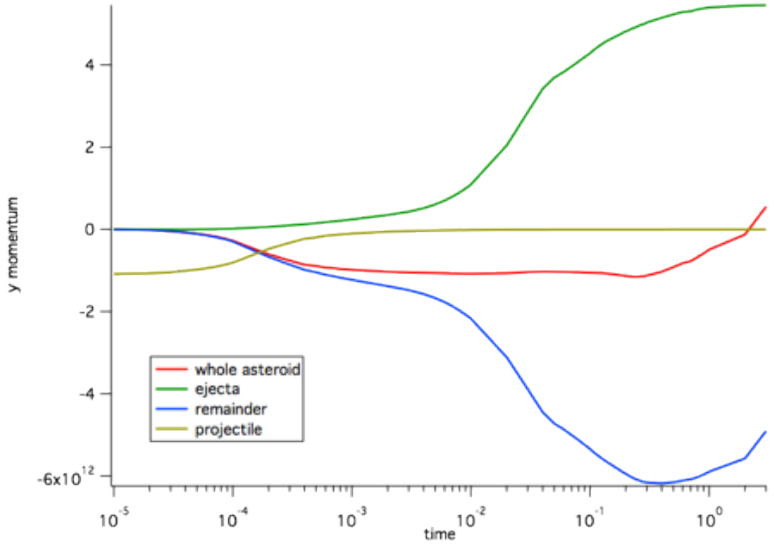

Fig. 31.— (LANL) Time-history plot of mesh-averaged axial momenta for the asteroid and projectile materials in run eD18. Transfer of momentum between projectile and asteroid occurs within the first millisecond, and the ejecta boil off subsequently, boosting the negative axial velocity of the remaining asteroid material.

The exchange of momentum between the projectile and the asteroid begins immediately upon contact, and by about 2×10^{-4} seconds, momentum is shared equally between the two. By a few milliseconds, the bulk asteroid has essentially all the momentum that the projectile originally had, and the ejecta from the crater are beginning to move away. Ejecta continue boiling away from the crater location, enhancing the push delivered to the remainder of the asteroid. The momentum enhancement factor β increases steadily during this period, Eventually, boundary effects come into play, as well as sharing of momentum with the included, but nonphysical, background gas.

Results from the two methods of calculating β are reported in Table 4. At high porosities, both methods agree in reporting β in the range 2-5. At porosities lower than about 20%, much higher and less reliable values are reported by both methods. Porosities for real asteroids are expected to be fairly high, so we are confident in predicting values of 2-5 for dry, stony asteroids. The presence of volatiles is expected to increase these values.

5.2. Spheral Results (LLNL, *M. Bruck-Syal*)

All Spheral calculations were carried out in three-dimensions (3D) using a lattice node generator and 10^6 - 10^7 particles. The characteristic smoothing length for these simulations was 44.5 cm. The time evolution of momentum transfer was tracked until β values converged. Calculating β in Spheral is carried out using two independent methods, as shown in Figure 32. The first method sums the momentum of ejecta exceeding escape velocity (e.g., $v_{\rm escape}$ = 6.086 cm/s for full-density SiO_2), and the second method tracks the center-of-mass for gravitationally bound material. The two methods are in good agreement, converging to the same value, as seen in the time evolution of β in the Figure 32 example.

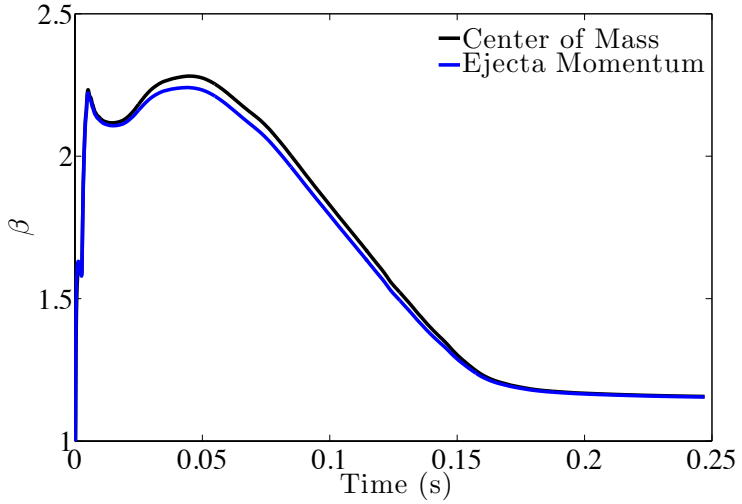

Fig. 32.— (LLNL) Comparison of two different methods for calculating the momentum multiplication factor, β: tracking the asteroid's center of mass (black) and summing the momentum of ejecta exceeding escape velocity (blue). The two methods yield very similar results throughout the simulated time; final values for β are nearly identical ($< 0.2\%$ difference).

Using the ILTP-specified material parameters, including 0% porosity, no strength, and a Mie Gruneisen equation of state, results in β values that are significantly larger than predicted for more realistic material properties. For the 0% porosity case (using a strengthless Mie Gruneisen representation of SiO_2) produces $\beta = 31.5$; for 40% porosity, $\beta = 8.0$. A more widely used equation of state for planetary impact modeling is ANEOS (Thompson 1972; Melosh 2007) which is able to capture melt and vapor transitions in a thermodynamically consistent manner. The effects of varying equations of state on β were recently examined by Bruck-Syal et al. (2016). Using the ANEOS or LEOS (Fritsch 2011) equations of state for SiO_2 asteroids resulted in lower β values than for the Tillotson equation of state (Tillotson 1962), which is very similar to the Mie Gruneisen representation (see Figure 33). Furthermore, including even a small amount of asteroid strength was found to dramatically decrease β, as seen in Figure 34. The presence of porosity also lowers β, as illustrated in Figure 35.

Table 5: (LLNL) List of Kinetic Impact Simulations

No.	v_i [a]	m_i [b]	D_a [c]	EOS[d]	Y_0 [e]	Porosity[f]	P [g]	Resolution (cm)[h]	β
1	10	10	50	T	NS	0.4	-	32.1	3.507
2	10	10	50	L	NS	0.4	-	32.1	3.087
3	10	10	50	A	NS	0.4	-	32.1	2.898
4	10	10	50	T	VM, 3.5 GPa	0.4	-	32.1	2.243
5	10	1	100	A	NS	0.4	-	44.5	5.432
6	10	1	100	A	1 kPa	0.4	-	44.5	3.695
7	10	1	100	A	10 kPa	0.4	-	44.5	3.693
8	10	1	100	A	100 kPa	0.4	-	44.5	3.569
9	10	1	100	A	1 MPa	0.4	-	44.5	1.917
10	10	1	100	A	10 MPa	0.4	-	44.5	1.301
11	10	1	100	A	50 MPa	0.4	-	44.5	1.196
12	10	1	100	A	100 MPa	0.4	-	44.5	1.094
13	10	1	100	A	VM, 100 MPa	0.4	-	44.5	1.112
14	10	1	100	A	1 kPa	0.0	-	44.5	5.230
15	10	1	100	A	1 kPa	0.05	-	44.5	4.159
16	10	1	100	A	1 kPa	0.1	-	44.5	4.096
17	10	1	100	A	1 kPa	0.2	-	44.5	4.000
18	10	1	100	A	1 kPa	0.3	-	44.5	3.898
19	10	1	100	A	1 kPa	0.5	-	44.5	3.571
20	10	1	100	A	100 MPa	0.0	-	44.5	1.249
21	10	1	100	A	100 MPa	0.1	-	44.5	1.155
22	10	1	100	A	100 MPa	0.2	-	44.5	1.138
23	10	1	100	A	100 MPa	0.3	-	44.5	1.101
24	10	1	100	A	100 MPa	0.5	-	44.5	1.077
25	5	10	50	T	NS	0.4	100	32.1	3.022
26	5	10	50	T	NS	0.4	-	32.1	2.965
27	5	10	50	T	VM, 3.5 GPa	0.4	100	32.1	1.822
28	5	10	50	T	VM, 3.5 GPa	0.4	-	32.1	1.858
29	5	5	100	L	100 MPa	0.4	9000	38.1	1.225
30	5	5	100	L	100 MPa	0.4	-	38.1	1.223
31	1	1	100	A	1 kPa	0.4	-	44.5	2.494
32	3	1	100	A	1 kPa	0.4	-	44.5	3.330
33	5	1	100	A	1 kPa	0.4	-	44.5	3.567
34	20	1	100	A	1 kPa	0.4	-	44.5	4.654
35	30	1	100	A	1 kPa	0.4	-	44.5	5.945

[a] impact velocity (km/s)

[b] impactor mass (10^3 kg)

[c] asteroid diameter (m)

[d] T: Tillotson, L: LEOS, A: ANEOS

[e] Strength takes form of Equation 2, except NS: no strength, VM: von Mises

[f] $\rho_0 = 2.65$ g/cm^3

[g] Rotation Period (s)

[h] Convergence occurs near 15 cm; 44.5-cm resolution may over-estimate β by ∼12.25%

5.3. Conclusions for ILTP1i Code-to-Code Comparison (*M. Bruck-Syal, G. Gisler*)

Despite using vastly different numerical methods, the results for ILTP1i from RAGE and Spheral, which calculated β for a 1 ton, 10 km/s impact on a full-density, strengthless SiO_2 sphere, compare quite well: $\beta_R = 31$ for RAGE and $\beta_S = 31.5$ for Spheral, yielding only a 1.6% difference. However, the inclusion of approximately the same amount of porosity (38% in RAGE and 40% in Spheral) resulted in significantly different results: $\beta_R = 3.73$ and $\beta_S = 7.96$. These calculations were not formally part of the ILTP1 but conducted out of interest. This discrepancy could be related to the different porosity models used: Spheral utilizes a strain-based porosity model (Wünnemann et al. 2006) while RAGE uses a p-α porosity model (Herrmann 1969). It could also be related to resolution differences: while Spheral used constant 44.5-cm spatial resolution, RAGE's Adaptive Mesh Refinement allows variable mesh resolution throughout the problem. Additionally, the problem was constructed in a 2-D axisymmetric geometry in RAGE but a fully 3-D geometry in Spheral. Axisymmetric geometry may introduce on-axis artifacts, which could possibly affect the β computation results.

Future ILTPs may benefit from explicit comparison of the time evolution of β between the two codes, to see how β converges and at what times, particularly since a variety of methods can be used to calculate β. Additionally, future comparative work can build upon these initial problems to use increasingly realistic asteroid material properties. Most of the deflection calculations in Spheral (Table 5) have been carried out using the ANEOS equation of state, as it is more commonly used in the planetary impact literature. Mie Gruneisen was used for ILTP1i because it is one of the few solid equation of state options that is built into both RAGE and Spheral. Adding in comparisons across a range of reasonable porosities and strengths would lend additional insight to possible variations between results from the two codes.

6. Summary (*K. Howley*)

The NNSA Laboratories and NASA have joined in an interagency collaboration to study mitigation strategies to prevent asteroid collisions with Earth. As part of this task, LANL and LLNL have been tasked with a code-to-code comparison of our modeling capabilities to explore the response of an asteroid-like target to a deflection attempt. In this report, LANL and LLNL developed, simulated and compared an inter-laboratory test problem (ILTP1) to verify modeling capabilities of the effects of nuclear explosions (ILTP1n, ILTP1x) and kinetic impactors (ILTP1i) on asteroid-like objects. We find that for stand-off nuclear explosions we achieve good agreement for the neutron particle transport and deposition into the asteroid-like surface. However, larger deviations in the overall response of the target and resulting deflection velocities are seen. We conclude that these differences are primarily due to the resolution of the hydrodynamic mesh, and that, with an appropriate meshing scheme, better agreement can be achieved. For kinetic impactors, we report good agreement in the momentum multiplication factor β for our test object.

However, with the introduction of porosity, and hence more complex physics modeling, the results begin to deviate.

Acknowledgements

LLNL-JRNL-XXXXXX. This work was performed under the auspices of the U.S. Department of Energy by Lawrence Livermore National Laboratory under Contract DE-AC52-07NA27344.

REFERENCES

Benz, W. & Asphaug, E. (1994). Impact simulations with fracture. I. Method and tests. In: Icarus.

Benz, W. & Asphaug, E. (1995). Simulations of brittle solids using smooth particle hydrodynamics. In: Computer physics communications.

Bruck-Syal, M. et al. (2016). Deflection by kinetic impact: sensitivity to asteroid properties. Icarus, In press

Caramana, E. J., Burton, D. E. & Shashkov, M. J. (1998). The construction of compatible hydrodynamics algorithms utilizing conservation of total energy. In: Journal of Computational Physics 146, pp. 227-262.

European Space Agency (ESA) (2015), http://www.esa.int/Our_Activities/Space_Engineering_Technology/NEO/Asteroid_Impact_Deflection_Assessment_AIDA_study

Fritsch, F. N. (2011). LIP: The Livermore Interpolation Package, Version 1.4. Lawrence Livermore National Laboratory, Livermore, CA, LLNL-TR-406719-REV-3

Gittings, M. et al. (2009). Computational Science and Discovery, 1, 015005.

Grüneisen, E. (1912). Theorie des festen Zustandes einatomiger Elemente. In: Annalen der Physik 344(12), pp. 257-306.

Hergenrother, C. W. et al. (2014). The Design Reference Asteroid for the OSIRIS-REx Mission Target (101955) Bennu. In: arXiv:1409.4704

Herrmann, W., (1969). Constitutive equation for the dynamic compaction of ductile porous materials, Journal of Applied Physics, 40, 2490–2499

Howley, K., Managan, R. & Wasem, J. (2014), Blow-off momentum from melt and vapor in nuclear deflection scenarios, Acta Astronautica, 103, pp. 376-381

Housen, K. R. & Holsapple, K. A. (2012). Deflecting Asteroids by Impacts: What is Beta? 43rd Lunar and Planetary Science Conference, LPI Contribution No. 1659, id.2539

Melosh, H. J. (2007). A Hydrocode Equation of State for SiO_2, Meteoritics & Planetary Science, 42, Nr12, 20792098

Mie, G. (1903). Zur kinetischen Theorie der einatomigen Körper. In: Annalen der Physik 316.8, pp. 657-697.

Monaghan, J. J. (2005). Smoothed particle hydrodynamics. In: Reports on progress in physics.

Movshovitz, N. et al. (2015). Disruption and reaccretion of midsized moons during an outer solar system Late Heavy Bombardment. In: Geophysical Research Letters 42.2, pp. 256-263.

Owen, J. M. (2010). ASPH modeling of Material Damage and Failure. In: Proceedings of the 5 th International SPHERIC Workshop. Manchester, UK, pp. 297-304.

Owen, J. M. (2014). A compatibly differenced total energy conserving form of SPH. In: International Journal for numerical methods in fluids 75.11, pp. 749-774.

Owen, J. M., Miller, P., et al. (2015). Asteroid Diversion Considerations and Comparisons of Diversion Techniques. In: Procedia Engineering 103, pp. 466-474.

Owen, J. M., Villumsen, J. V., et al. (1998). Adaptive Smoothed Particle Hydrodynamics: Methodology. II. In: The Astrophysical Journal Supple- ment Series 116.2, pp. 155-209.

Richet, S. & Bottinga, P., Thermochemical Properties of Silicate Glasses and Liquids: A Review, Rev. Geophys., 24, 125, 1986

Thompson, S. L. & Lauson, H. S., (1972). Improvements in the Chart D Radiation Hydrodynamic Code III: Revised Analytical Equation of State, Sandia National Laboratory, SC-RR-710714

Thompson, S. L., (1990). ANEOS Analytic Equations of State for Shock Physics Codes Input Manual, Sandia National Laboratory, Albuquerque, NM, SAND892951

Tillotson, J. H. (1962). Metallic Equations of State for Hyper-Velocity Impact. In: General Atomics Report.

Wünnemann, K., Collins, G. & Melosh, H. (2006). A strain-based porosity model for use in hydrocode simulations of impacts and implications for transient crater growth in porous targets.

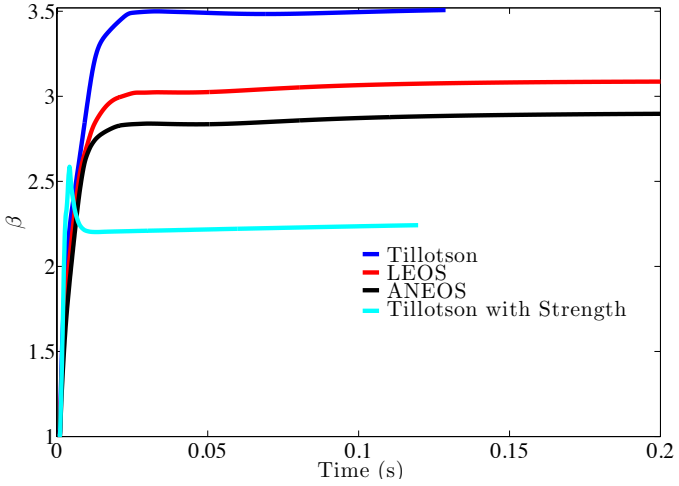

Fig. 33.— (LLNL) Momentum multiplication factor, β, plotted as a function of time for kinetic-impact simulations, using three different SiO_2 equations of state: Tillotson (Tillotson 1962), LEOS (Fritsch 2011), and ANEOS (Thompson 1972; Melosh 2007). To simplify comparison, no strength or damage models were initially included (blue, red, black lines). Including strength (cyan line) reduces β significantly. Momentum delivery converges to a final value within the first $\sim$ 0.2 s. While Tillotson is a simpler analytic equation of state and useful under a range of lower-velocity impact conditions, LEOS and ANEOS capture melting and vaporization processes more accurately.

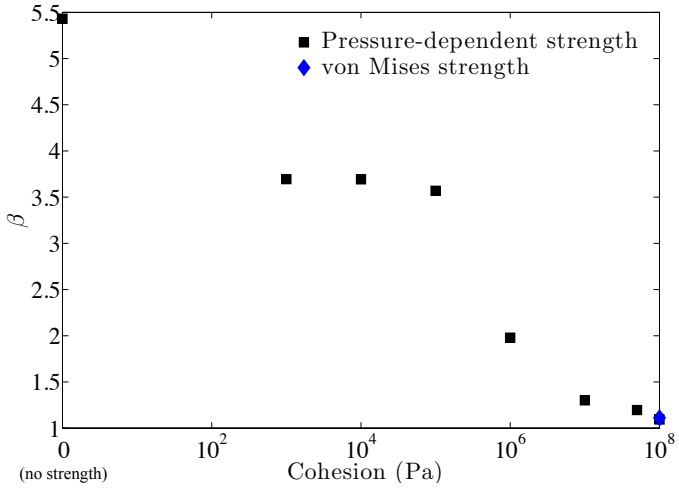

Fig. 34.— (LLNL) Increasing values of cohesion for asteroid material decreases the momentum enhancement factor, β, for kinetic deflections. Modeling the asteroid as strengthless results in a significant over estimate: $\beta \sim 5.5$. Cohesion values representative of weak soils (1 kPa) to weak rocks (100 kPa) produce similar deflection velocities, while somewhat larger values of cohesion (1-100 MPa, representative of stronger rocks), lead to increasingly smaller values for β. Use of a constant (von Mises criterion) strength for the 100 MPa case produced a slightly larger β value than the pressure-dependent strength model; the latter is considered more accurate and used in the majority of the simulations. ANEOS and 40% porosity used for all simulations.

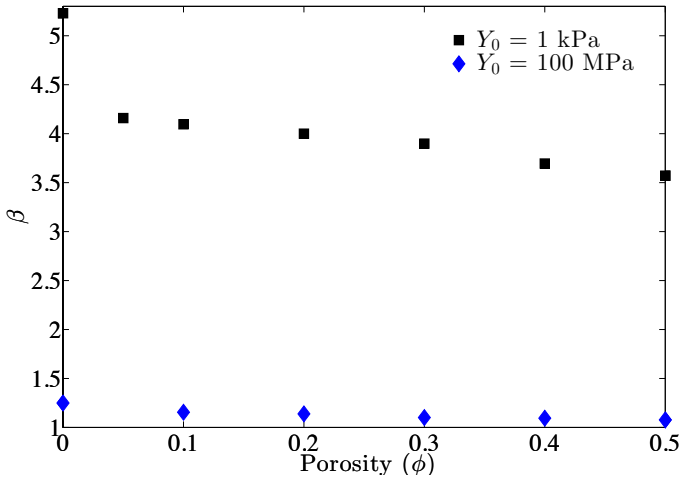

Fig. 35.— (LLNL) The presence of microporosity decreases the total momentum of target material ejected during an impact, reducing β. The effects of varying asteroid porosity on delivered momentum impulse are shown for different values of cohesion: $Y_0 = 1$ kPa and $Y_0 = 100$ MPa. For the low-cohesion cases, there is an abrupt decrease in β between nonporous and slightly porous ($\phi = 0.05$) material and a more gradual decrease with further increasing microporosity. For the high-cohesion cases, porosity effects on momentum transfer are less prominent. ANEOS used for all simulations.